Article

Ultrahigh-Ionic-Conductivity, Antifreezing Poly(amidoxime)-Grafted Polyzwitterion Hydrogel for Facile Integrated into High-Performance Stretchable Flexible Supercapacitor

Zhiyuan Peng, Yutang Zhou, Honghao Shu, Chuying Yu, and Wenbin Zhong*

Read Online

ACCESS | Metrics & More | Article Recommendations | SI Supporting Information

ABSTRACT: Developing wearable supercapacitors (SCs) with high stretchability, arbitrary deformability, and antifreezing ability is still a challenge. In the present work, an ultrahigh-ionic-conductivity, antifreezing poly(amidoxime)-*graft*-polyzwitterion (PAO-*g*-PSBMA) hydrogel electrolyte is fabricated by grafting PSBMA in PAO. Owing to the abundant hydrophilic and high ionic adsorption capacity of amidoxime groups in PAO and zwitterion groups in PSBMA, the as-prepared PAO-*g*-PSBMA hydrogel can facilitate the dissociation of lithium salt and exhibit an ultrahigh ionic conductivity of 29.8 S m^{-1} at 25 °C and 3.4 S m^{-1} even at −30 °C. Employing $m_A Ti_3C_2T_x$ and $m_S Ti_3C_2T_x$, which contain small amounts of PAO-AGE and PAO-*g*-PSBMA dispersions, respectively, coated onto both sides of the PAO-*g*-PSBMA hydrogel, we followed a thermal treatment to facilely form integrated stretchable flexible SCs. The as-prepared SCs show an outstanding recoverable tensile stain of 80% and an excellent electrochemical stability under many types and times of arbitrary deformation. More importantly, as-prepared $m_A Ti_3C_2T_x$- and $m_S Ti_3C_2T_x$-based SCs present fantastic antifreezing ability and excellent stability with 74.6 and 78.3% retention of the initial capacitance, respectively, even after 1000 times of stretching to 60% at −30 °C. This work offers a new strategy of using PAO-grafted polyzwitterion for obtaining an antifreezing stretchable SC, which shows a high potential for application in next-generation integrated stretchable devices in various fields.
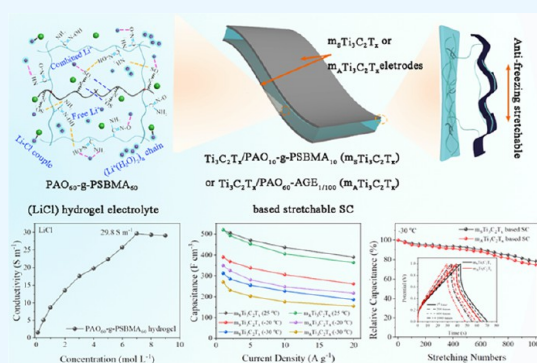
1. INTRODUCTION

With the rapid development of portable and wearable electronic devices, flexible or even stretchable energy storage systems with high energy storage capacity, robust mechanical properties, and wearing safety are demanded.[1−3] As one of the main energy supplies, wearable supercapacitors (SCs) continue to be a highly active research field owing to their superior power density, fast charging/discharging rate, long cycle life, and ease of manufacture.[4] Over the past decades, tremendous efforts have been devoted to fabricate wire/fiber-like electrodes via electrospinning and paper-like electrodes via anchoring electroactive materials on a paper/textile or any other flexible substrate, and construct three-dimensional porous flexible electroactive film electrodes and then combined them with a gel electrolyte separator to construct flexible SCs.[5,6] These SCs exhibit stable electrochemical properties under arbitrary deformations (such as bending, twisting, folding, etc.).[7] However, there are growing requirements for a highly stretchable electronic skin, strain sensors, light-emitting diodes, display panels, and other stretchable devices, which promote the development of stretchable SCs acting as essential energy storage components.[8−11] Up to now, the stretchability of stretchable SCs mainly depends on the ion-conductive hydrogel electrolytes (such as vinyl hybrid silica nano-

particle-polyacrylamide (PAM)/H$_3$PO$_4$, poly(2-acrylamido-2-methylpropanesulfonic acid-*co*-N,N-dimethylacrylamide)/laponite/graphene oxide, etc.), which can be prestretched and then coated on electroactive materials to construct stretchable SCs.[12−14] The conductive polymers can be grown on the stretchable hydrogel electrolytes (such as boron cross-linked poly(vinyl alcohol) (PVA)/KCl) by in situ polymerization to form stretchable SCs.[15] In addition, employing stretchable electrodes to construct stretchable SCs was also reported, such as the stretchable electrodes prepared by paving a CNT film onto a prestretched polydimethylsiloxane substrate, the stretchable PVA@polypyrrole@silver nanowires foam electrodes.[16,17] Unfortunately, these single-component stretchable SCs usually suffer from mechanical mismatches and vulnerably beget sliding and delamination under large deformations or the electrodes contain a large number of nonelectroactive polymer substrates, thus delivering a poor rate capacity (the capacitance
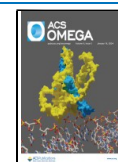
retention is usually less than 30% at the current density of 1–20 mA cm^{-2}), low stretch strains (<100% without prestretch), and/or stretch cycle stabilities (the capacitance retention of prestretched stretchable SC is < 80% after 1000 stretching cycles).[11–18] To solve these issues, efforts have also been paid to the research of integrated stretchable SCs with intrinsically stretchable electrodes and electrolyte. The integrated stretchable SCs are assembled using stretchable polypyrrole-incorporated gold nanoparticles/CNT/PAM hydrogel electrodes and a gold nanoparticle/PAM/Na$_2$SO$_4$ hydrogel electrolyte. Owing to the excellent compatibility of PAM and dynamic Au-thiolate bonds between the electrodes and electrolyte, the SC exhibits good antidelamination ability and excellent capacitance stability during stretching (the strain ranging from 0 to 800%).[19] However, the electrodes contain a high content of nonelectroactive PAM and the SC exhibits low rate capacities (capacitance retention of 66% at a current density of 1–9 mA cm^{-2}). Furthermore, to apply SCs at harsh temperature, integrated stretchable SCs with excellent antifreezing ability are highly demanded, but there are only a few recent reports on these.[20,21] More recently, a stretchable antifreezing flexible SC was prepared by in situ growth of polyaniline onto a PAM/ethylene glycol/water/H$_2$SO$_4$ electrolyte, which showed a rate capacity of 74.3% at a current density from 0.03 to 0.6 mA cm^{-2} and could be repeatedly stretched to a strain of 200% for 100 cycles without significant capacitance loss at −30 °C.[20] The stretchable AgNW/Ag-CNT/PAM hydrogel electrodes and PAM/ethylene glycol/H$_2$O/LiCl electrolyte were assembled into an integrated stretchable SC, which showed a rate capacity of 85.1% at a current density ranging from 1 to 9 mA cm^{-2} at −35 °C and maintained 80.9% of the initial capacitance when stretched with strains from 0 to 800% at −35 °C.[21] While the antifreezing ability of the stretchable SCs mainly depends on the organic ethylene glycol antifreeze agent, which can interact with water molecules and disturb the formation of hydrogen bonds and then hinder the generation of ice crystal lattices under low temperature, the organic agents are un-ionized and volatile, which lead to a low ionic conductivity and easy leakage, and cause security problems.[22] Accordingly, it is still a great challenge to construct integrated stretchable SCs with excellent rate capacity, antifreezing ability, high ionic conductivity, and environmental friendliness.

In a polymer ion-conductive hydrogel, the polymeric network components present outstanding biocompatibility and mechanical flexibility and even stretchability, and capture the electrolyte ions to promote the dissociation of metal salts, and hence are ideal candidates as implanted bioelectronics, proton exchange membranes, electronic skin, and energy storage device electrolytes.[23–26] In general, polymer ion-conductive hydrogels are composed of cross-linked hydrophilic polymer networks and a salt/acid/alkali solution: e.g., PVA/Zn(CF$_3$SO$_3$)$_2$, bacterial cellulose/PAM/H$_2$SO$_4$, poly(acrylic acid)/CaCO$_3$/laponite, P(AM-co-2-(dimethylamino)ethyl methacrylate)/gelatin/LiCl.[27–31] These ion-conductive hydrogels exhibit excellent flexibility but show a relatively low ionic conductivity (<8 S m^{-1}) owing to the limited ion dissociation capacity of the functional group in polymer chains. To achieve the high-ionic-conductivity hydrogels, polymers that can strongly interact with ions to improve the ion dissociation capacity have been employed. Different kinds of polymer ion-conductive hydrogels, such as the anionic polymer-based hydrogels (sodium polyacrylate/cellulose/KOH, PVA/nega-

tively charged carboxymethyl cellulose/NaCl),[32,33] the cationic polymer-based hydrogels (carboxymethyl cellulose/methacrylamidopropyltrimethylammonium chloride/PAM/Li$_2$SO$_4$),[34] and the polyzwitterion-based hydrogels (cellulose-g-poly-(sulfobetaine methacrylate) (PSBMA)/NaCl, P(AM-co-SBMA)/(Zn(OTf)$_2$)), have been constructed.[35,36] These polymer ion-conductive hydrogels exhibit a relatively high ionic conductivity from 8 to 20 S m^{-1},[33–36] even up to 28 S m^{-1}.[32] Although some high-ionic-conductivity hydrogels at room temperature have been constructed, they may not work at subzero temperatures because the large amount of water in the hydrogel network will inevitably freeze, hence leading to the quick drop of conductivity.[37,38] To meet the application requirements under low temperatures, there is a need of developing an ion-conductive hydrogel with suitable antifreezing property. At present, antifreezing ion-conductive hydrogels have been prepared by introducing organic antifreeze agents (such as ethylene glycol, glycerin, dimethyl sulfoxide, etc.) into polymer ion-conductive hydrogels.[39–41] However, the low conductivity (less than 1 S m^{-1} at −30 °C) and volatile and/or toxicity limit their practical application.[42] Alternatively, the hydrophilic polymer chains (containing such as −NH$_2$, −OH, zwitterion groups, etc.) in an ion-conductive hydrogel can interact with water molecules, disturb the formation of hydrogen bonds among the water molecules, and inhibit the generation of ice crystal lattices exhibiting antifreeze abilities.[43–46] Although antifreezing ion-conductive hydrogels have made some progress, developing high-ionic-conductivity hydrogels under low temperatures still faces challenges.

Polyamidoxime (PAO), containing amidoxime groups composed of -NH$_2$ and −OH, possesses excellent chelating abilities of metal ions. Although PAO-based membranes and hydrogels (such as Fe@polydopamine-PAO membrane, Zn^{2+}-PAO hydrogel, chitosan-PAO hydrogel etc.) are widely used in heavy metal adsorption,[47–49] they are rarely reported as ion-conductive hydrogel electrolytes. In our recent work, a PAO/polyethylenimine hydrogel has been prepared through hydrogen bond interactions, which shows an ultrahigh ionic conductivity of 19.1 S m^{-1} in 6 M LiCl and 22.35 S m^{-1} in 6 M KOH.[50] SBMA is a charged polymer having unique zwitterionic groups in its repeat units, which exhibits high water retention abilities, solubility, and electrostatic interaction with metal ions.[35,36] Thus, SBMA can be applied to construct excellent ion-conductive hydrogels and antifreezing materials.[45] Recently, the SBMA-2-hydroxyethyl acrylate copolymer hydrogel with LiCl showed a high ionic conductivity of 1.26 S m^{-1} at −40 °C.[46] Motivated by the demand for antifreezing and stretchable energy storage devices, an antifreezing integrated stretchable supercapacitor was fabricated using poly(amidoxime)-graft-polyzwitterion (PAO-g-PSBMA) hydrogel as the electrolyte and modified Ti$_3$C$_2$T$_x$ as electrodes. The PAO-g-PSBMA ion-conductive hydrogel was prepared by chemical modification followed by a grafting polymerization process. The abundant amidoxime groups in PAO and zwitterion groups in PSBMA chains facilitate the dissociation of the lithium salt, leading to a high ionic conductivity of 29.8 S m^{-1} in 7 M LiCl, and the ion migration mechanism was discussed, assisted by an in situ atomic force microscope (AFM). A modified Ti$_3$C$_2$T$_x$ dispersion was coated on the surface of the as-prepared PAO-g-PSBMA hydrogel. Benefiting from the strong interactions (e.g., cross-linking, entanglement, H-bonds) between the electrodes and electrolyte, the modified Ti$_3$C$_2$T$_x$ hydrogel in situ anchored tightly on the PAO-g-
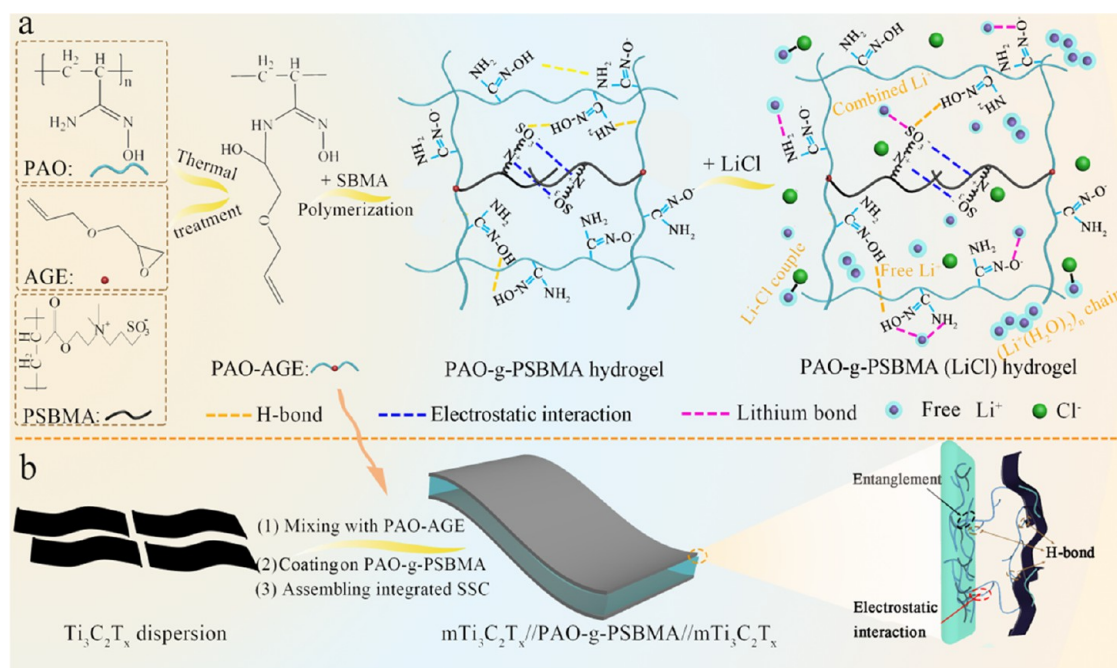
Figure 1. (a) Illustration of the preparation process of the PAO_{60}-g-$PSBMA_{60}$ hydrogel electrolyte and proposed mechanism of the high dissociation capacity of LiCl in the PAO_{60}-g-$PSBMA_{60}$ hydrogel. (b) Fabrication process of the $mTi_3C_2T_x$//PAO_{60}-g-$PSBMA_{60}$//$mTi_3C_2T_x$ integrated stretchable SC and illustration of the interaction between $Ti_3C_2T_x$ electrodes and the hydrogel electrolyte.

PSBMA hydrogel during the thermal treatment process. Therefore, as-prepared stretchable SCs are expected to deliver excellent stretchability, antifreezing ability, and energy storage property.

2. RESULTS AND DISCUSSION

The fabrication process of the ultrahigh-ionic-conductivity, stretchable PAO_{60}-g-$PSBMA_{60}$ hydrogel electrolyte is illustrated in Figure 1a. First, the AGE undergoes a ring-opening reaction with PAO in the TBAOH solution (10 wt %) to form PAO-AGE during thermal treatment. Then, the PAO_{60}-g-$PSBMA_{60}$ hydrogel electrolyte is prepared by one-step grafting polymerization of SBMA into PAO-AGE for AGE possessing polymerizable double bonds. In the PAO_{60}-g-$PSBMA_{60}$ matrix, the 3D network structure is constructed by physical entanglement among polymer chains, hydrogen bonds, and electrostatic interactions among functional units,[48,52] which endow the as-prepared hydrogel excellent stretchability and elasticity (Figure 1a). When the PAO_{60}-g-$PSBMA_{60}$ hydrogel was soaked repeatedly in 7 M LiCl solution, a slight swelling could be observed due to the partial dissociation of hydrogen bonds and ionic bonds by the salt-in effect.[53] In the high-concentration LiCl (7 M) solution, Li exists in polymer-like $(Li^+(H_2O)_2)_n$ chains, $Li^+(H_2O)_4$, $Li_2^+(H_2O)_6$, Li−Cl couple, and free Li^+.[54,55] When the 7 M LiCl solution is introduced into the PAO_{60}-g-$PSBMA_{60}$ hydrogel, the lithium ions can chelate with amidoxime groups, the lithium bonds can form between the amino and hydroxyl groups in PAO with Li^+, and electrostatic interaction occurs between the zwitterions and Li^+ and Cl^-. These interactions make it easy for the Li salts in the system to dissociate,[36,46,48] which leads to the $(Li^+(H_2O)_2)_n$ polymer-like chains in high-concentration LiCl being unlocked into $Li^+(H_2O)_4$, $Li_2^+(H_2O)_6$, Li−Cl couple, and free Li^+.[54,55] In addition, the small-size hydrated Li ion and free ions are more easy for transmission. Based on the above-mentioned

interactions, the as-prepared PAO_{60}-g-$PSBMA_{60}$ with 7 M LiCl hydrogel electrolyte exhibits high ion transport capacity and ultrahigh ionic conductivity under the action of an applied electric field. The preparation process of $m_STi_3C_2T_x$//PAO_{60}-g-$PSBMA_{60}$//$m_STi_3C_2T_x$ and $m_ATi_3C_2T_x$//PAO_{60}-g-$PSBMA_{60}$//$m_ATi_3C_2T_x$ integrated stretchable flexible SCs is shown in Figure 1b; the $Ti_3C_2T_x$/PAO-AGE and $Ti_3C_2T_x$/PAO_{10}-g-$PSBMA_{10}$ dispersions were coated on both sides of the PAO_{60}-g-$PSBMA_{60}$ hydrogel. Owing to the excellent hydrophilicity and liquidity, a small number of PAO-AGE and PAO_{10}-g-$PSBMA_{10}$ polymer chains may permeate into the PAO_{60}-g-$PSBMA_{60}$ hydrogel. During the thermal treatment, the permeated polymer chains can tightly link with the PAO_{60}-g-$PSBMA_{60}$ hydrogel molecules by hydrogen bonds, physical entanglement, and electrostatic interactions. Moreover, both PAO-AGE and PAO_{10}-g-$PSBMA_{10}$ can interact with $Ti_3C_2T_x$ by hydrogen bonds and electrostatic interactions. Thus, the sandwich-structure stretchable combined hydrogel was constructed (Figure 1b). After soaking in 7 M LiCl solution, the integrated stretchable flexible SCs can be obtained.

^{1}H NMR spectra were recorded to verify the successful modification of PAO with AGE to form PAO_{60}-$AGE_{1/100}$ (Figure S1). Compared with PAO, new peaks at 5.83 and 5.18 ppm can be observed, which are assigned to the ethylenic protons H-4 and H-5, respectively,[56] suggesting the existence of double bonds in PAO_{60}-$AGE_{1/100}$. In addition, a weaker −NH_2 signal with peak at 3.47 ppm was shown in the curve of PAO_{60}-$AGE_{1/100}$ than that in PAO, and a new resonance peak belonging to −NH− appeared at 3.84 ppm.[42] Thus, the −NH_2 in PAO has been reacted with AGE and PAO_{60}-$AGE_{1/100}$ has been successfully synthesized.

The Fourier transform infrared (FT-IR) spectra of PAO, SBMA, PAO_{60}-$AGE_{1/100}$, and PAO_{60}-g-$PSBMA_{60}$ are presented in Figure 2a. Compared with the spectra of PAO, the characteristic peak at 1610 cm^{-1} is observed in PAO_{60}-$AGE_{1/100}$, corresponding to the C═C bond, indicating that
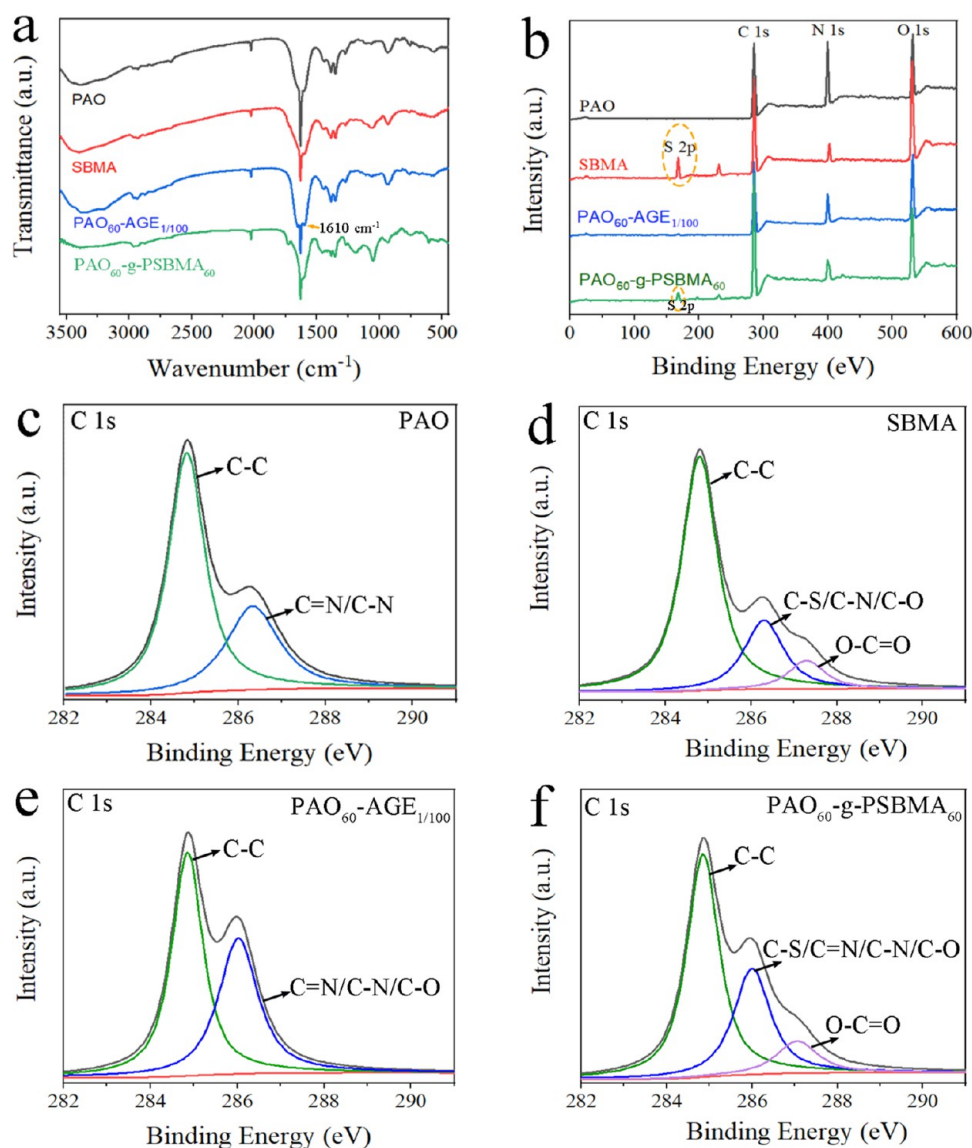
Figure 2. (a) FT-IR spectra and (b) X-ray photoelectron spectroscopy (XPS) spectra of PAO, SBMA, PAO_{60}-$AGE_{1/100}$, and PAO_{60}-g-$PSBMA_{60}$. The C 1s spectra of (c) PAO, (d) SBMA, (e) PAO_{60}-$AGE_{1/100}$, and (f) PAO_{60}-g-$PSBMA_{60}$.

AGE was modified in PAO.[42] Compared with PAO_{60}-$AGE_{1/100}$, additional peaks at 1178 and 645 cm^{-1} corresponding to the $-SO_3^-$ stretching vibration can be observed for PAO_{60}-g-$PSBMA_{60}$,[35,52] suggesting the presence of PSBMA. In addition, the peaks observed at 1365, 3367, and 1051 cm^{-1} can be assigned to the C−N stretching vibration, −OH stretching vibration, and C−O−C stretching vibration, respectively,[35] which can be observed in the spectrum of PAO_{60}-g-$PSBMA_{60}$, implying the successful graft of PSBMA in the PAO chain.

The elemental compositions of the as-prepared samples were analyzed by X-ray photoelectron spectroscopy (XPS) and the related chemical compositions are listed in Table S1. As shown in Figure 4b, compared with PAO, the lower content of N 1s and higher content of O 1s peaks can be observed in PAO_{60}-$AGE_{1/100}$, indicating the coexistence of PAO and AGE. Compared to the N content of PAO_{60}-$AGE_{1/100}$ (at. 14.32%), the PAO_{60}-g-$PSBMA_{60}$ shows a lower N content (at. 9.13%). Meanwhile, attributed to the introduction of PSBMA, a new S 2p peak can be found in PAO_{60}-g-$PSBMA_{60}$, which suggests that the SBMA has been grafted in PAO_{60}-$AGE_{1/100}$. Besides,

PAO_{60}-g-$PSBMA_{60}$ exhibits a higher O content (22.1 atom %) than that of PAO_{60}-$AGE_{1/100}$, which further indicates the presence of SBMA. Figure 2c−f presents the C 1s peaks of PAO, SBMA, PAO_{60}-$AGE_{1/100}$, and PAO_{60}-g-$PSBMA_{60}$. The C 1s peak can be deconvoluted into three peaks, with the peaks at 284.7, 286.3, and 287.5 eV corresponding to C−C/C=C, C−S/C−O/C−N/C=N, and O−C=O, respectively.[36,50] Obviously, the relative content of C=N/C−N for PAO_{60}-$AGE_{1/100}$ (36.62 atom %) is higher than that of PAO (26.71 atom %) (Figure 2c,e). This result is attributed to the high content of C−O in the introduced AGE (Figure 2d). Additionally, the PAO_{60}-g-$PSBMA_{60}$ shows a lower C−S/C−O/C−N/C=N content (32.32 atom %) than that of PAO_{60}-$AGE_{1/100}$ (Figure 2e), suggesting that the SBMA with low C−S/C−O/C−N content (22.71 atom %) is grafted in PAO_{60}-$AGE_{1/100}$.

Figure 3 shows the optical images, in situ atomic force microscope (AFM) images of microstructures, and current changes for the PAO_{60}-g-$PSBMA_{60}$ hydrogel and PAO_{60}-g-$PSBMA_{60}$ with 7 M LiCl hydrogel electrolyte. From the optical
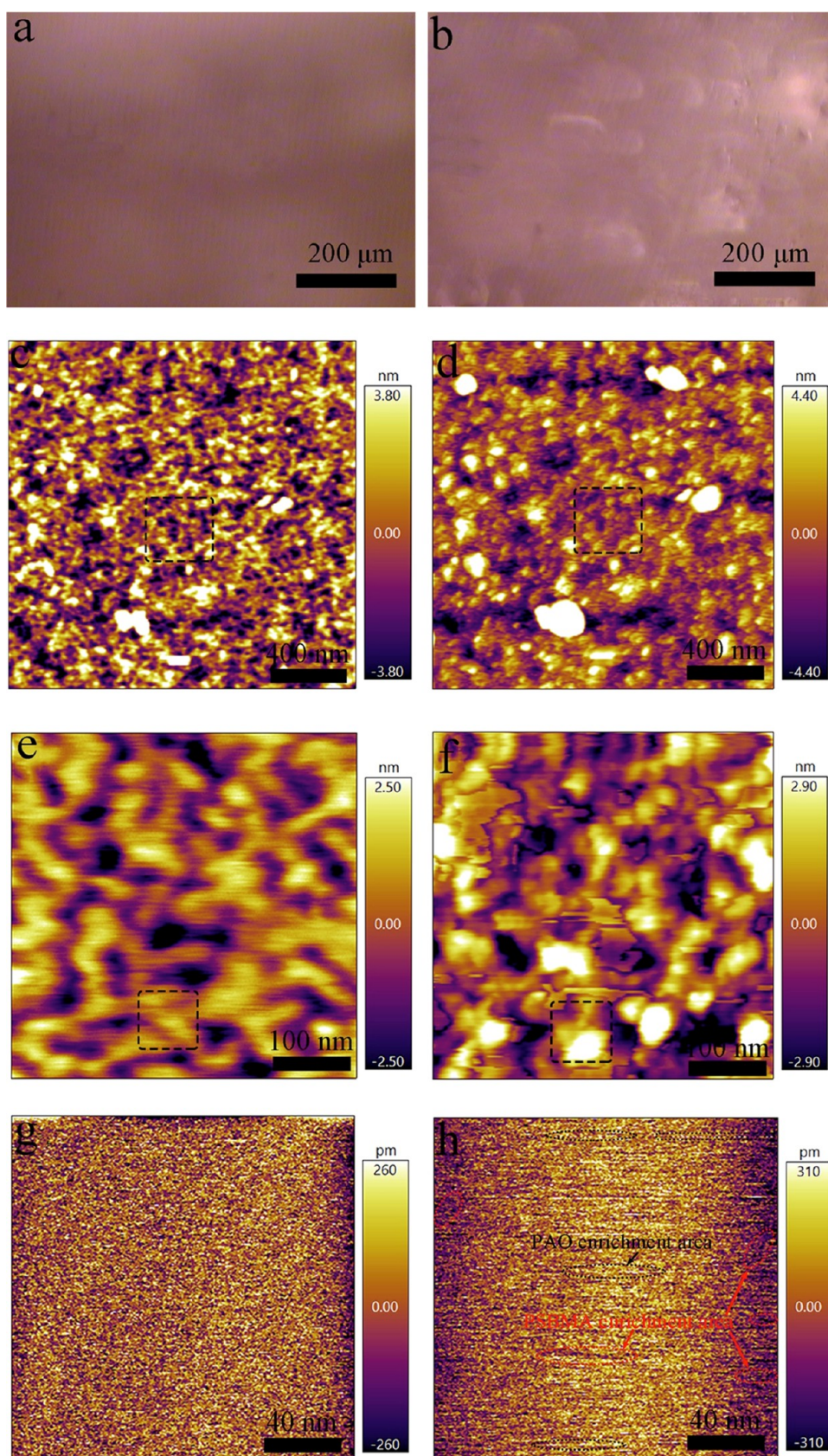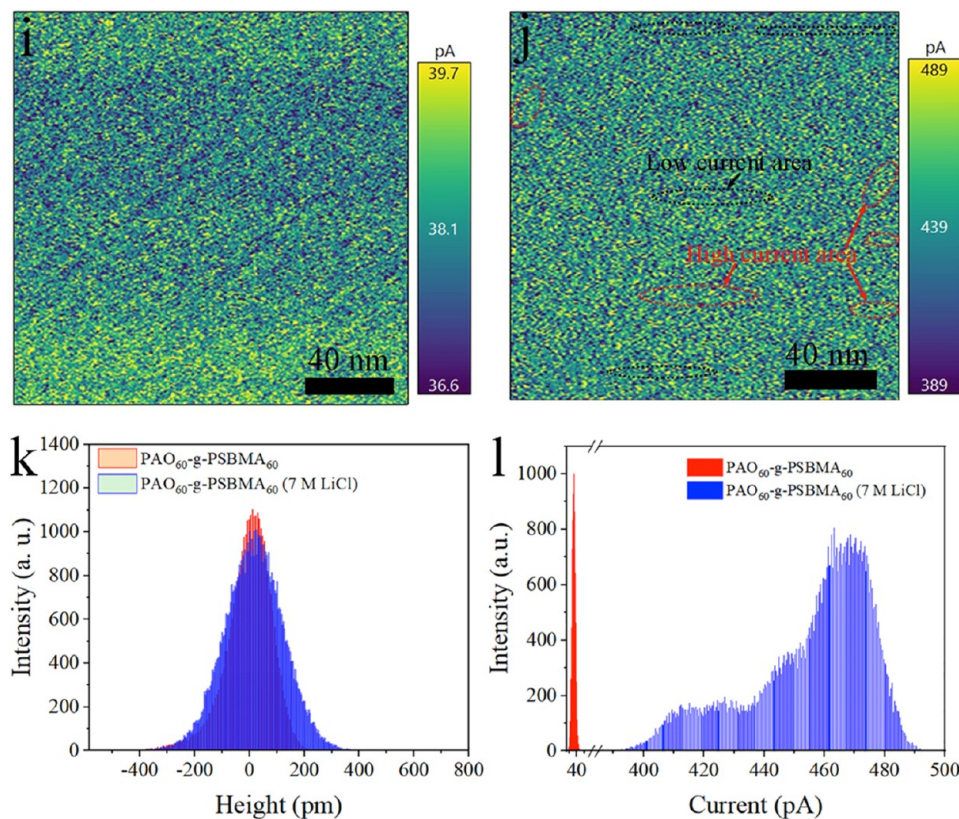
Figure 3. continued

Figure 3. Optical image of PAO_{60}-g-$PSBMA_{60}$ hydrogel (a) and with 7 M LiCl (b). The AFM height images of the PAO_{60}-g-$PSBMA_{60}$ hydrogel (c, e) and with 7 M LiCl (d, f) under different magnifications. The AFM height images of the PAO_{60}-g-$PSBMA_{60}$ hydrogel (g) and (h) 7 M LiCl using the conductive mode. The c-AFM for the current images of the PAO_{60}-g-$PSBMA_{60}$ hydrogel (i) without LiCl and (j) with LiCl. The histograms of (k) height and (l) current distributions of PAO_{60}-g-$PSBMA_{60}$ hydrogel without and with LiCl.

images, the PAO_{60}-g-$PSBMA_{60}$ hydrogel exhibits a smooth surface (Figure 3a) and no pores and defects can be observed. When LiCl was introduced into the PAO_{60}-g-$PSBMA_{60}$ hydrogel system, some bulges can be observed on the surface of the hydrogel, which may be attributed to the reduction of the number of hydrogen bonds and ionic bonds among the PAO_{60}-g-$PSBMA_{60}$ hydrogel as LiCl is introduced (Figure 3b).[53] To investigate the influence of LiCl on the microstructure and current of the PAO_{60}-g-$PSBMA_{60}$ hydrogel, the in situ topographical, amplitude, and phase images of AFM are obtained by tapping mode in the same area by the in situ technique as shown in Figures 3c−f and S2−S4. In the AFM images of the PAO_{60}-g-$PSBMA_{60}$ hydrogel (Figure 3c), there are apparently separated bright and dark domains corresponding to the relatively harder PAO and relatively softer PSBMA, respectively.[57] In the phase image (Figure S4a), the relatively bigger viscous PSBMA domain is brighter than the PAO domain, presenting two different phases.[58] In addition, the height deviation between the bright and dark domains is measured to be about 7.6 nm, while a higher height deviation of 8.8 nm can be observed after soaking in 7 M LiCl (Figures 3d and S4b), which is attributed to the partial dissociation of hydrogen bonds and ionic bonds among polymers, leading to rougher surfaces and swelling of the hydrogel. The high-magnification AFM images of the PAO_{60}-g-$PSBMA_{60}$ hydrogel with/without LiCl (Figures 3e,f, S4, and S5) also exhibit uniform distribution of PAO and PSBMA. Figure 3g−j shows the in situ conductive AFM (c-AFM) images of the PAO_{60}-g-$PSBMA_{60}$ hydrogel with/without LiCl. For the PAO_{60}-g-$PSBMA_{60}$ hydrogel, the bright and dark phases are uniformly

distributed in the image (Figure 3g), corresponding to PAO and PSBMA domains, respectively. However, after soaking with 7 M LiCl (Figure 3h), the darker domains increase obviously and the height deviations between bright and dark domains become larger (Figure 3k), demonstrating that LiCl can partially dissociate the hydrogen bonds and ionic bonds in hydrogel.

The current image of the PAO_{60}-g-$PSBMA_{60}$ hydrogel exhibits a homogeneous current distribution with a low average current of about 38.1 pA (Figure 3i), which may be related to the low concentration of ions. For the PAO_{60}-g-$PSBMA_{60}$ hydrogel with 7 M LiCl, the current image shows a homogeneous current increase and exhibits an average current of about 439 pA (Figure 3j), which demonstrate that both of the active groups in PAO and PSBMA can promote the dissociation of Li salts and improve the ion transport capacity in the applied electric field. In addition, from the histograms of the current distribution (Figure 3l), after the hydrogel is soaked in 7 M LiCl, the current exhibits a clear two-stage distribution. Meanwhile, compared with the height and current images of the PAO_{60}-g-$PSBMA_{60}$ hydrogel (Figure 3h−j), the PAO enrichment area (bright domain) and PSBMA enrichment area (dark domain) in the height image (Figure 3h) correspond to the low current area and high current area in the current image (Figure 3j), respectively. Thus, PSBMA may possess a higher capability of capture and dissociation ion than PAO.

The compression stress−strain curves of PAO_{60}-g-$PSBMA_{60}$, PAO_{60}-g-$PSBMA_{60}$ (7 M LiCl), and $PAO_{60}/PSBMA_{60}$ hydrogels are shown in Figure 4a, and the compression stress−strain
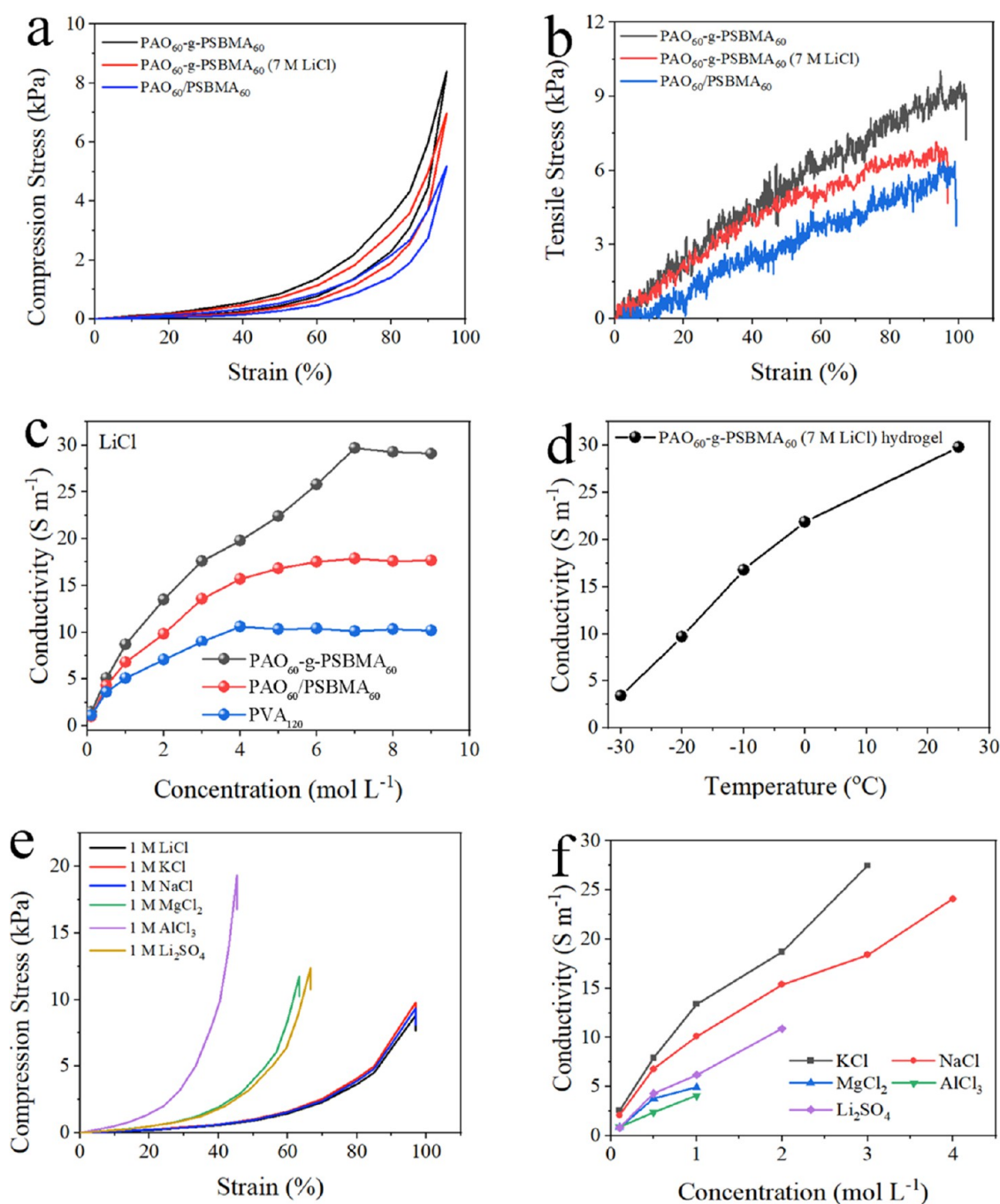
Figure 4. (a) Compressive and (b) tensile stress−strain curves of PAO_{60}-g-$PSBMA_{60}$, PAO_{60}-g-$PSBMA_{60}$ (7 M LiCl), and PAO_{60}/$PSBMA_{60}$ hydrogels. (c) Ionic conductivity of PAO_{60}-g-$PSBMA_{60}$, PAO_{60}/$PSBMA_{60}$, and PVA hydrogels with different concentrations of LiCl solution. (d) Ionic conductivity of PAO_{60}-g-$PSBMA_{60}$ (7 M LiCl) hydrogel at different temperatures. (e) Compression stress−strain curves and (f) ionic conductivity of PAO_{60}-g-$PSBMA_{60}$ hydrogel with different metal salt solutions (the concentration is influenced by the solubility).

curves of PAO_x-AGE_y-$PSBMA_z$ hydrogels are shown in Figure S7a. All of the hydrogel samples prepared for the tests were in cylindrical shape with a smooth surface. Additionally, it is found that PAO_{120} and $PSBMA_{120}$ homopolymers cannot form a hydrogel (Figure S6). Compared with the compression stress−strain curves and conductivity of PAO_x-AGE_y-$PSBMA_z$ hydrogels with different component contents in Figure S7, it is found that the compression strength of PAO_{60}-g-$PSBMA_{60}$ is low but the crack strain almost remains unchanged, while the compression strength and crack strain of PAO_{60}-g-$PSBMA_{80}$ are low. Additionally, the crack strain of PAO_{60}-$AGE_{1/50}$-

$PSBMA_{60}$ is low when the content of AGE increases (Figure S7a). However, the conductivity of the as-prepared hydrogel increases along with the content of PSMBA (Figure S7b). Considering the compression strength, elasticity, and conductivity of as-prepared hydrogels, the PAO_{60}-$AGE_{1/100}$-$PSBMA_{60}$ hydrogel is determined as the optimal sample. As demonstrated in Figure 4a, all of the PAO_{60}-g-$PSBMA_{60}$, PAO_{60}-g-$PSBMA_{60}$ (7 M LiCl), and PAO_{60}/$PSBMA_{60}$ hydrogels can withstand a recoverable compression strain of up to 95%. The corresponding stresses are 4.8, 8.3, and 7.1 kPa for PAO_{60}/$PSBMA_{60}$, PAO_{60}-g-$PSBMA_{60}$, and PAO_{60}-g-$PSBMA_{60}$
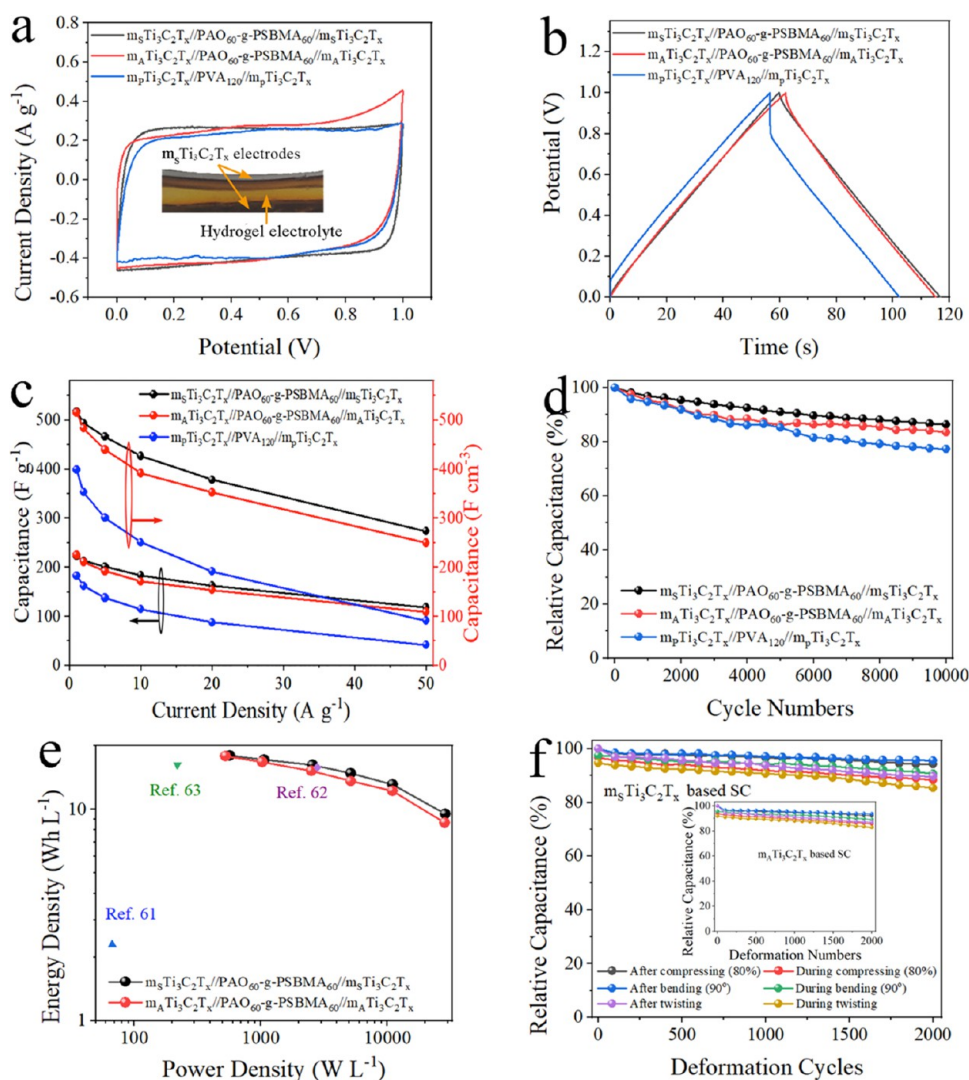
Figure 5. (a) CV curves of $m_STi_3C_2T_x//PAO_{60}$-g-$PSBMA_{60}//m_STi_3C_2T_x$-, $m_ATi_3C_2T_x//PAO_{60}$-g-$PSBMA_{60}//m_ATi_3C_2T_x$-, and $m_pTi_3C_2T_x//PVA_{120}//m_pTi_3C_2T_x$-based SCs at a scan rate of 5 mV s^{-1}. (b) GCD curves of as-prepared SCs at a current density of 1 A g^{-1}. (c) Specific capacitance and volumetric capacitance at different current densities. (d) Cycling tests at a current density of 10 A g^{-1} for 10,000 cycles. (e) Ragone plot of $m_STi_3C_2T_x//PAO_{60}$-g-$PSBMA_{60}//m_STi_3C_2T_x$- and $m_ATi_3C_2T_x//PAO_{60}$-g-$PSBMA_{60}//m_ATi_3C_2T_x$-based SCs. (f) Capacitance retention of $m_STi_3C_2T_x//PAO_{60}$-g-$PSBMA_{60}//m_STi_3C_2T_x$- and $m_ATi_3C_2T_x//PAO_{60}$-g-$PSBMA_{60}//m_ATi_3C_2T_x$-based SCs during 2000 times of cyclic compressing strain of 80%, bending of 90°, and twisting process.

(7 M LiCl) hydrogels, respectively. The sharper increase of the compression strength for the PAO_{60}-g-$PSBMA_{60}$ hydrogel than that of $PAO_{60}/PSBMA_{60}$ is attributed to the grafted PSBMA in PAO_{60}-$AGE_{1/100}$, which can generate a strong interaction and enhance the strength of the hydrogel. The compression strength of the PAO_{60}-g-$PSBMA_{60}$ (7 M LiCl) hydrogel is lower than that of the PAO_{60}-g-$PSBMA_{60}$ hydrogel, because a large number of Li$^+$ can dissociate the hydrogen bonds and ionic bonds among polymer chains, hence causing the strength decrease.[53] Impressively, the strength of the PAO_{60}-g-$PSBMA_{60}$ (7 M LiCl) hydrogel is almost undamaged after 1000 cycles of compression under a compression strain of 95% (Figure S8a). Meanwhile, the PAO_{60}-g-$PSBMA_{60}$ hydrogel presents a high tensile strength of 9.6 kPa with the breaking elongation of 102% (Figure 4b), which is higher than that of the PAO_{60}-g-$PSBMA_{60}$ (7 M LiCl) hydrogel (6.7 kPa, ε = 97%) and $PAO_{60}/PSBMA_{60}$ hydrogel (5.8 kPa, ε = 99%). When a large tensile strength is imposed, the formation and propagation of cracks can be delayed due to the applied stress being dispersed

by the strong interaction in the hydrogel, resulting in a high elongation at break.[50] Thus, the tensile strength of the PAO_{60}-g-$PSBMA_{60}$ (7 M LiCl) hydrogel is almost unchanged after 1000 cycles of stretching under a tensile strain of 80% (Figure S8b). The ionic conductivity of PAO_{60}-g-$PSBMA_{60}$, $PAO_{60}/PSBMA_{60}$, and PVA_{120} hydrogels at different concentrations of LiCl solutions is measured at room temperature. As shown in Figures 4c and S9, the ionic conductivity of the PAO_{60}-g-$PSBMA_{60}$ hydrogel increases along with the LiCl salt concentration. A threshold appears when the LiCl concentration is 7 mol L^{-1}, indicating that the combination of anionic, amino, and hydroxyl groups with Li$^+$, as well as cationic groups with Cl$^-$ is saturated. Also, the conductivity of the PAO_{60}-g-$PSBMA_{60}$ hydrogel reaches up to 29.8 S m^{-1}, which is higher than that of $PAO_{60}/PSBMA_{60}$ (16.8 S m^{-1}) (7 mol L^{-1} LiCl) and PVA_{120} (10.2 S m^{-1}) (4 mol L^{-1} LiCl) hydrogels, and is superior to those of the PSBMA/HEA/LiCl hydrogel (14.6 S m^{-1})[46] and PANa-cellulose (KOH) hydrogel (28 S m^{-1});[32] more details are listed in Table S2. The high ionic conductivity

of the PAO_{60}-g-$PSBMA_{60}$ hydrogel is attributed to the interaction of PAO and PSBMA with ions promoting the dissociation of Li salts, and the hydrophilic grafting polyzwitterion network decreases the crystallinity of polymers and increases the ion-conducting chains.[59] In addition, the PAO_{60}-g-$PSBMA_{60}$ hydrogel with 7 M LiCl exhibits excellent water retention performance (Figure S10a). Importantly, the hydrophilic PAO and PSBMA chains can interact with water molecules, disturb the formation of hydrogen bonds among water molecules, and inhibit the generation of ice crystal lattices. Thus, the PAO_{60}-g-$PSBMA_{60}$ (7 M LiCl) hydrogel presents a high ionic conductivity of 3.4 S m^{-1} even under −30 °C for 8 h (Figures 4d and S11). In addition, the differential scanning calorimetry (DSC) measurements were performed to analyze the frozen state of the hydrogel samples, and the results of the PAO_{60}-g-$PSBMA_{60}$ hydrogel without and with 7 M LiCl are shown in Figure S10b. Although the PAO_{60}-g-$PSBMA_{60}$ hydrogel can show a slightly low temperature resistance due to the interaction of the abundant amidoxime groups of PAO and zwitterionic groups of SBMA with water, an obvious melting peak can be observed at around −3.4 °C, indicating that most of the water in the hydrogel is still "free water" and can be easily frozen. After immersing in 7 M LiCl, the peak appeared at about −48.2 °C. Furthermore, the PAO_{60}-g-$PSBMA_{60}$ (7 M LiCl) hydrogel at −30 °C exhibits a similar mechanical compressibility to that at 25 °C (Figure S10c). These results suggest that the water in the PAO_{60}-g-$PSBMA_{60}$ (7 M LiCl) hydrogel electrolyte is mostly "unfrozen water" that cannot be frozen at low temperatures. To expand our understanding on the proposed approach, different metal salts were introduced into the PAO_{60}-g-$PSBMA_{60}$ network to obtain PAO_{60}-g-$PSBMA_{60}$-Mn hydrogels, where Mn represents metal salts (1 M LiCl, NaCl, KCl, $MgCl_2$, $AlCl_3$, and Li_2SO_4). The compression stress−strain curves of the PAO_{60}-g-$PSBMA_{60}$-Mn hydrogels are shown in Figure 4e. All of the PAO_{60}-g-$PSBMA_{60}$-Mn hydrogels exhibit different levels of high compression strength compared to the PAO_{60}-g-$PSBMA_{60}$ with LiCl hydrogel. In contrast with chlorine salts, monovalent Na$^+$, K$^+$, and Li$^+$ ions show negligible influence on the compression strength and crack strain. The PAO_{60}-g-$PSBMA_{60}$ with 1 M $AlCl_3$ hydrogel has the highest compression strength of 19.8 kPa due to the synergy of ionic and metal−ligand bonds.[48,60] The PAO_{60}-g-$PSBMA_{60}$-Li_2SO_4 hydrogel shows a compression strength of 12.4 kPa at the crack strain of 66%. This result is attributed to the kosmotropic anions of SO_4^{2-} enhancing the hydrogen bonds among polymer chains, resulting in the compression strength increasing as the strain decreases.[53] The ionic conductivity of PAO_{60}-g-$PSBMA_{60}$-M hydrogels is shown in Figure 4f. Influenced by the solubility, the PAO_{60}-g-$PSBMA_{60}$ with NaCl and KCl hydrogel, respectively, exhibit the highest ionic conductivity of 23.2 S m^{-1} (4 M NaCl) and 28.1 S m^{-1} (3 M KCl). Compared with PAO_{60}-g-$PSBMA_{60}$ with LiCl, the high ionic conductivity of the hydrogel electrolyte could be attributed to the low combination of Na$^+$ and K$^+$ with water, which is easy for transmission.[32] While the PAO_{60}-g-$PSBMA_{60}$-$MgCl_2$, PAO_{60}-g-$PSBMA_{60}$-$AlCl_3$, and PAO_{60}-g-$PSBMA_{60}$-Li_2SO_4 hydrogels exhibit a low conductivity of 4.9 S m^{-1} (1 M $MgCl_2$), 4.3 S m^{-1} (1 M $AlCl_3$), and 11.2 S m^{-1} (2 M Li_2SO_4), respectively, which may be due to the relatively low concentration of the salt, the high metal−ligand bonds between the large-sized Mg^{2+}/Al^{3+} and polymers, and the salt-out effect of SO_4^{2-} lead

to the active hydrophilic groups decreasing and the polymer chain becoming rigid; thus, salt ions are hard to transmit.[53]

$Ti_3C_2T_x$/PAO_{60}-$AGE_{1/100}$ and $Ti_3C_2T_x$/PAO_{10}-g-$PSBMA_{10}$ dispersions were coated, respectively, on both surfaces of the as-prepared PAO_{60}-g-$PSBMA_{60}$ hydrogel to obtain $m_A Ti_3C_2T_x$/PAO_{60}-g-$PSBMA_{60}$/$m_A Ti_3C_2T_x$ and $m_S Ti_3C_2T_x$/PAO_{60}-g-$PSBMA_{60}$/$m_S Ti_3C_2T_x$ sandwich-like structure hydrogel, respectively (Figure S12). The $m_S Ti_3C_2T_x$ and $m_S Ti_3C_2T_x$ hydrogels can be tightly combined, which is because the polymer chains in the dispersion can permeate into the PAO_{60}-g-$PSBMA_{60}$ hydrogel and are tightly linked with PAO_{60}-g-$PSBMA_{60}$ hydrogel molecules by hydrogen bonds, physical entanglement, and electrostatic interactions (Figure S13). Furthermore, $Ti_3C_2T_x$ can strongly interact with PAO_{60}-$AGE_{1/100}$ and $Ti_3C_2T_x$/PAO_{60}-g-$PSBMA_{60}$, respectively, due to the hydrogen bonds and electrostatic interactions (Figure S14). Additionally, $Ti_3C_2T_x$ cannot form an intact hydrogel when $Ti_3C_2T_x$ without polymer dispersion is coated on the surface of the PAO_{60}-g-$PSBMA_{60}$ hydrogel after thermal treatment (Figure S15). The as-prepared $m_S Ti_3C_2T_x$/PAO_{60}-g-$PSBMA_{60}$/$m_S Ti_3C_2T_x$, $m_A Ti_3C_2T_x$/PAO_{60}-g-$PSBMA_{60}$/$m_A Ti_3C_2T_x$, and $m_p Ti_3C_2T_x$/PVA_{120}/$m_p Ti_3C_2T_x$ hydrogels were soaked with 7 M LiCl to construct a stretchable flexible SC. As shown in Figure 5a, the CV curves of the as-prepared SCs present the typical rectangular-like shape corresponding to the ideal double-layer capacitive behavior.[16,31] There is no obvious deviation of the rectangular-like shape and the low potential curve is completely included within the curve in the potential window of 0−1.0 V, indicating good capacitive characteristics (Figure S16). Rectangular-like shapes are well maintained for $m_S Ti_3C_2T_x$//PAO_{60}-g-$PSBMA_{60}$//$m_S Ti_3C_2T_x$ and $m_A Ti_3C_2T_x$/PAO_{60}-g-$PSBMA_{60}$/$m_A Ti_3C_2T_x$ even at an extremely high scan rate of 100 mV s^{-1}, indicating a good reversibility and quick charge transfer capability (Figure S17).[29] Figure 5b shows the GCD curves of the as-prepared SCs. It can be found that the GCD curves of $m_S Ti_3C_2T_x$- and $m_A Ti_3C_2T_x$-based SCs demonstrated a nearly triangular shape without obvious voltage drop, while the $m_p Ti_3C_2T_x$-based SC exhibits a large IR drop of 0.28 V, suggesting that the $m_S Ti_3C_2T_x$- and $m_A Ti_3C_2T_x$-based SCs have low internal resistance. In addition, the $m_S Ti_3C_2T_x$//PAO_{60}-g-$PSBMA_{60}$//$m_S Ti_3C_2T_x$ and $m_A Ti_3C_2T_x$//PAO_{60}-g-$PSBMA_{60}$//$m_A Ti_3C_2T_x$ show a volumetric specific capacitance of 519 and 517 F cm^{-3} (225 and 223 F g^{-1}) at a current density of 1 A g^{-1}, respectively (Figures 5c and S18), which is higher than that of $m_p Ti_3C_2T_x$//PVA_{120}//$m_p Ti_3C_2T_x$ (398 F cm^{-3}, 186 F g^{-1}). The $m_S Ti_3C_2T_x$//PAO_{60}-g-$PSBMA_{60}$//$m_S Ti_3C_2T_x$ and $m_A Ti_3C_2T_x$//PAO_{60}-g-$PSBMA_{60}$//$m_A Ti_3C_2T_x$ still retain a volumetric specific capacitance of 273 F cm^{-3} (52.6%) and 249 F cm^{-3} (48.1%) even at a high current density of 50 A g^{-1}, respectively, while $m_p Ti_3C_2T_x$//PVA_{120}//$m_p Ti_3C_2T_x$ only retains a specific capacitance of 91 F cm^{-3} (22.9%) at 50 A g^{-1}. In addition, with the increase of mass loading from 1 to 5 mg cm^{-2}, the gravimetric capacitance reduced by only 9.3% and maintained outstanding rate performance (Figure S19). The excellent rate capabilities of $m_S Ti_3C_2T_x$//PAO_{60}-g-$PSBMA_{60}$//$m_S Ti_3C_2T_x$ and $m_A Ti_3C_2T_x$//PAO_{60}-g-$PSBMA_{60}$//$m_A Ti_3C_2T_x$ are attributed to the 3D conducting networks of the modified $Ti_3C_2T_x$ electrodes, high ionic conductivity of the PAO_{60}-g-$PSBMA_{60}$ hydrogel electrolyte, and the tight combination of the electrodes and electrolyte, which facilitate the rapid ion diffusion and charge transport at high current densities.[19]
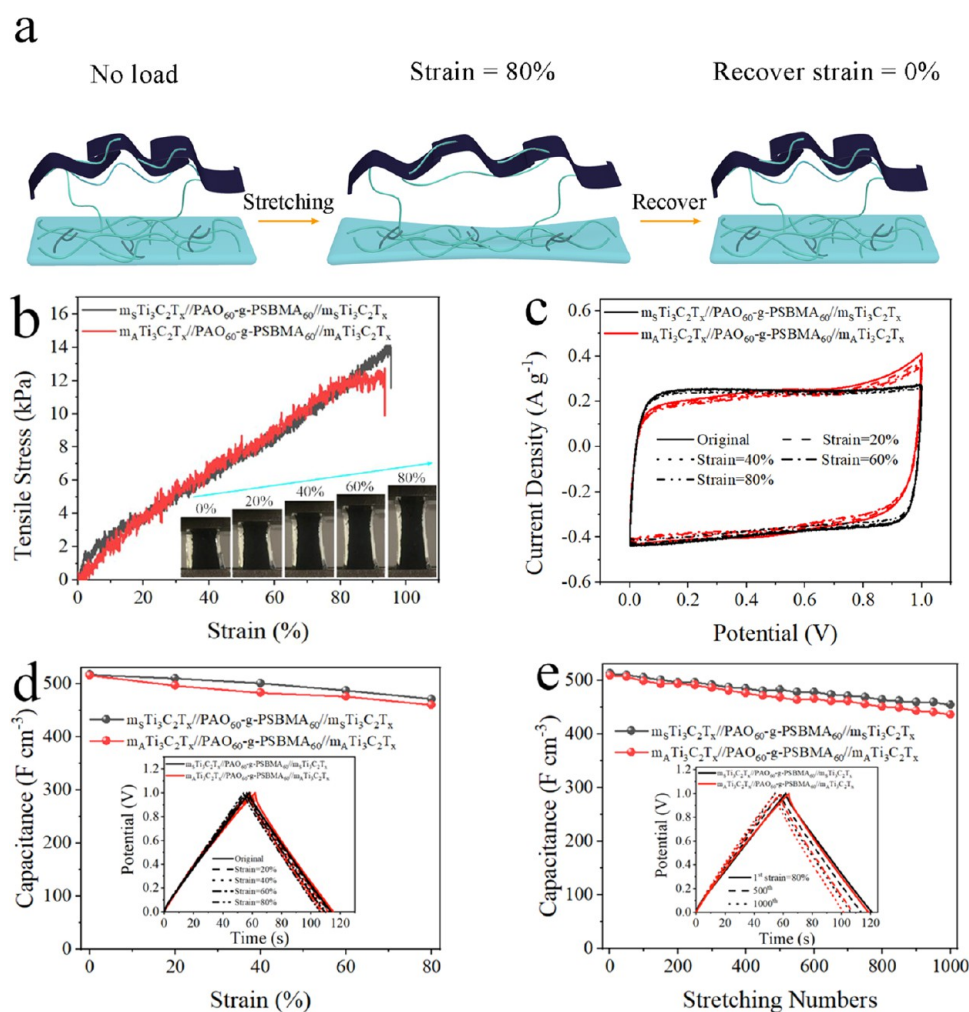
Figure 6. (a) Illustration of the stretching process and (b) tensile stress−strain curve of $m_S Ti_3 C_2 T_x$- and $m_A Ti_3 C_2 T_x$-based stretchable flexible SCs. (c) CV curves at the scan rate of 5 mV s^{-1} and (d) capacitance retention of $m_S Ti_3 C_2 T_x$ and $m_A Ti_3 C_2 T_x$ stretchable flexible SCs under different stretch strains. (e) Capacitance retention of $m_S Ti_3 C_2 T_x$ and $m_A Ti_3 C_2 T_x$ stretchable flexible SCs during cyclic stretching to a strain of 80% in 1000 cycles.

$m_S Ti_3 C_2 T_x$//PAO$_{60}$-g-PSBMA$_{60}$//$m_S Ti_3 C_2 T_x$ exhibits a higher rate capability than that of $m_A Ti_3 C_2 T_x$//PAO$_{60}$-g-PSBMA$_{60}$//$m_A Ti_3 C_2 T_x$, which is because the added PAO$_{60}$-g-PSBMA$_{60}$ has better compatibility with the hydrogel electrolyte than PAO$_{60}$-AGE$_{1/100}$, further promoting the ion transport.[21] The electrochemical stability of the as-prepared SCs was tested at a current density of 10 A g^{-1} for 10,000 cycles (Figures 5d and S20). $m_S Ti_3 C_2 T_x$//PAO$_{60}$-g-PSBMA$_{60}$//$m_S Ti_3 C_2 T_x$ and $m_A Ti_3 C_2 T_x$//PAO$_{60}$-g-PSBMA$_{60}$//$m_A Ti_3 C_2 T_x$ maintain 86.4 and 83.5% of the initial capacitance after 10000 charge/discharge cycles, respectively, which are higher than that of $m_p Ti_3 C_2 T_x$//PVA$_{120}$//$m_p Ti_3 C_2 T_x$ (77.3%). The excellent cycling stability of $m_s Ti_3 C_2 T_x$//PAO$_{60}$-g-PSBMA$_{60}$//$m_s Ti_3 C_2 T_x$ and $m_A Ti_3 C_2 T_x$//PAO$_{60}$-g-PSBMA$_{60}$//$m_A Ti_3 C_2 T_x$ can be attributed to the synergistic effect of the modified Ti$_3$C$_2$T$_x$ electrodes and PAO$_{60}$-g-PSBMA$_{60}$ electrolyte, as well as the superior ionic conductivity of the electrolyte. The Ragone plots of the $m_s Ti_3 C_2 T_x$//PAO$_{60}$-g-PSBMA$_{60}$//$m_s Ti_3 C_2 T_x$- and $m_A Ti_3 C_2 T_x$//PAO$_{60}$-g-PSBMA$_{60}$//$m_A Ti_3 C_2 T_x$-based SCs are illustrated in Figure 5e. The SCs exhibit the highest volumetric energy density of 17.9 and 17.8 Wh L^{-1} at a power density of 572 and 568 W L^{-1}, respectively, and maintain 9.4 and 8.6 Wh L^{-1} even at an ultrahigh power

density of 28678 and 28667 W L^{-1}, respectively. The energy storage capabilities of the as-prepared SCs are superior to those of the SCs based on the rGO/Ti$_3$C$_2$T$_x$ film (2.3 Wh L^{-1}, 67 W L^{-1}),[61] DA/rGO@PDA (16.3 Wh L^{-1}, 218.8 W L^{-1}),[62] and PANI-graphene hydrogel film (15.8 Wh L^{-1}, 2800 W L^{-1});[63] more details are listed in Table S4. Interestingly, the $m_s Ti_3 C_2 T_x$//PAO$_{60}$-g-PSBMA$_{60}$//$m_s Ti_3 C_2 T_x$- and $m_A Ti_3 C_2 T_x$//PAO$_{60}$-g-PSBMA$_{60}$//$m_A Ti_3 C_2 T_x$-based flexible SCs exhibit excellent flexibility and can sustain various repeated deformations. As shown in Figures 5f, S21, and S22, the capacitance of $m_s Ti_3 C_2 T_x$//PAO$_{60}$-g-PSBMA$_{60}$//$m_s Ti_3 C_2 T_x$-based SCs was retained at 94.1/96.3, 94.5/97.1, and 89.3/94.2% of the initial capacitance in the deformation/resuming state for repeated cyles of a compressing strain of 80%, bending of 90°, and twisting after 2000 cycles, respectively. The $m_A Ti_3 C_2 T_x$//PAO$_{60}$-g-PSBMA$_{60}$//$m_A Ti_3 C_2 T_x$-based SCs maintained 94.1/96.3, 94.5/97.1, and 89.3/94.2% of the initial capacitance at deformation/resuming state for repeated cycles of a compressing strain of 80%, bending of 90°, and twisting after 2000 cycles, respectively, suggesting that both as-prepared SCs show outstanding arbitrary deformable capability.
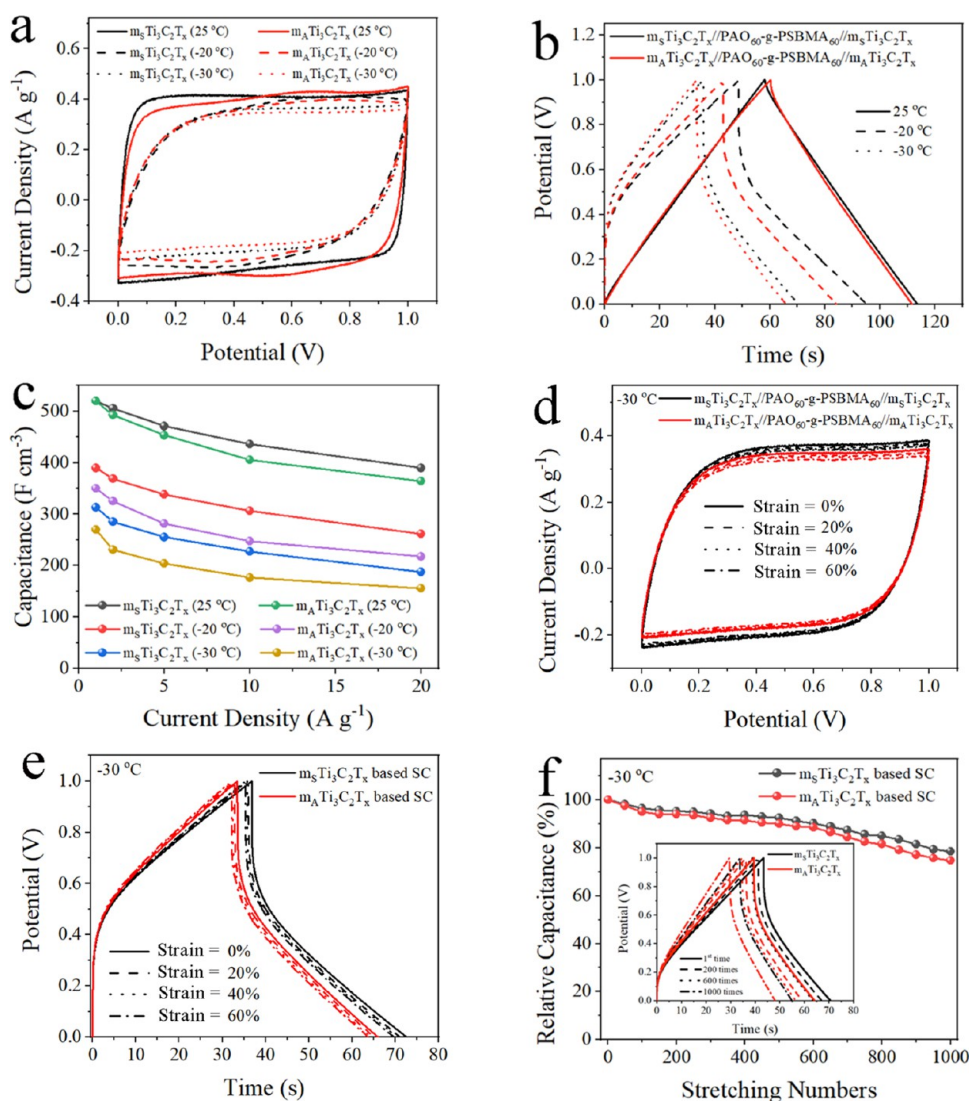
Figure 7. (a) CV and (b) GCD curves under different temperatures of $m_S Ti_3 C_2 T_x$- and $m_A Ti_3 C_2 T_x$-based stretchable flexible SCs. (c) Rate capacity of $m_S Ti_3 C_2 T_x$- and $m_A Ti_3 C_2 T_x$-based stretchable flexible SCs under different temperatures. (d) CV curves at the scan rate of 5 mV s^{-1} and (e) GCD curves of $m_S Ti_3 C_2 T_x$ and $m_A Ti_3 C_2 T_x$ stretchable flexible SCs under different stretching strains at −30 °C. (f) Capacitance retention of $m_S Ti_3 C_2 T_x$- and $m_A Ti_3 C_2 T_x$-based stretchable flexible SCs during stretching to a strain of 60% in 1000 cycles at −30 °C.

The excellent stretchability of the $m_S Ti_3 C_2 T_x$- and $m_A Ti_3 C_2 T_x$-based stretchable flexible SCs originates from their rational structure. The hydrogen bonds, physical entanglement, and electrostatic interactions between the modified $Ti_3 C_2 T_x$ electrodes and PAO$_{60}$-g-PSBMA$_{60}$ electrolyte endow the as-prepared SC a high structural integrity and stable electrical conductivity under stretched states. Since the external force could be evenly dissipated through the crinkling and spreading of polymer chains, the interface between the electrodes and the electrolyte cannot be separated by the stretching process (Figure 6a). The breaking elongation of the $m_S Ti_3 C_2 T_x$- and $m_A Ti_3 C_2 T_x$-based stretchable flexible SCs can reach up to 89.2 and 90.4%, respectively (Figure 6b). Furthermore, the CV and GCD curves of the $m_S Ti_3 C_2 T_x$- and $m_A Ti_3 C_2 T_x$-based stretchable flexible SCs are barely changed under stretch strains from 0 to 80% (Figure 6c,d), and up to 92.8 and 93.2% of their initial capacitance are retained when the devices are stretched to a strain of 80%, respectively (Figure 6d). The Nyquist plots of the $m_S Ti_3 C_2 T_x$-based stretchable flexible SC exhibit very similar curves at

different stretch strains, indicating that the variation of stretch strain has little influence on the diffusion of ions (Figure S23). In addition, negligible semicircles at high frequencies and vertical lines at low frequencies can be observed in the Nyquist plots, confirming the high conductivity and the ideal capacitive behavior of $m_S Ti_3 C_2 T_x$-based SCs under stretching. Furthermore, when the $m_S Ti_3 C_2 T_x$- and $m_A Ti_3 C_2 T_x$-based stretchable flexible SCs are repeatedly stretched to a strain of 80% and released after 1000 cycles, their stress−strain, CV, and GCD curves show negligible changes (Figures 6e, S24, and S25), and 88.4 and 85.6% of the initial capacitance is retained after 1000 stretch/release cycles, respectively.

Considering the practical application, SCs must work at low temperature. But many SCs cannot operate at subzero temperature, due to the reduced mobility and transport of the electrolyte ion with decrease of temperature. Herein, the as-prepared $m_S Ti_3 C_2 T_x$//PAO$_{60}$-g-PSBMA$_{60}$//$m_S Ti_3 C_2 T_x$ and $m_A Ti_3 C_2 T_x$//PAO$_{60}$-g-PSBMA$_{60}$//$m_A Ti_3 C_2 T_x$-based stretchable flexible SCs can deliver excellent electrochemical behaviors even at −30 °C. Figures 7a and S26 show the CV

curves of the as-prepared supercapacitor under different temperatures; the CV curves appear similar at different temperatures and the area is slightly reduced as the temperature decreases. The GCD curves of the as-prepared supercapacitor under different temperature are shown in Figure 7b. They can be found to be nearly triangular in shape and the little increase in *IR* drops due to the change of temperature that affects the diffusion rate of ions in the electrolyte. These results indicate the low influence of temperature on its capacitance behaviors. Besides, the capacitance of $m_S Ti_3C_2T_x$- and $m_A Ti_3C_2T_x$-based stretchable flexible SCs is 519/517, 398/357, and 317/272 F cm^{-3} under the current density of 1 A g^{-1} at 25, −20, and −30 °C, respectively (Figure 7c). Furthermore, the $m_S Ti_3C_2T_x$- and $m_A Ti_3C_2T_x$-based stretchable flexible SCs maintain capacitances of 211 (66.5% of the initial capacitance) and 167 (61.4%) F cm^{-3} under the current density of 20 A g^{-1} at −30 °C, respectively. The excellent rate performances are superior to those of the reported stretchable antifreezing integrated SCs based on PANI/AF−OHP/PANI (−30 °C, 73.1% (0.03−0.6 mA cm^{-2})),[20] graphene/PEDOT−PVA hydrogel fiber (−20 °C, 36% (0.1−1.6 A g^{-1})),[64] and AC//PSBMA/HEA//AC (−30 °C, 54% (1−5 mA cm^{-2}));[46] more details are listed in Table S3. The outstanding capacitance retention is ascribed to the hydrophilic PAO and PSBMA interacting with water molecules, which inhibits the generation of ice crystal lattices, and the electrolyte hydrogel promoting the dissociation of LiCl. Interestingly, the $m_S Ti_3C_2T_x$- and $m_A Ti_3C_2T_x$-based stretchable flexible SCs exhibit surprising stretchable abilities even under −30 °C. Figure 7d,e shows the CV and GCD curves of stretchable SCs with stretching strain from 0 to 60% under −30 °C, respectively, in which the electrochemical performance is almost identical even under a large stretching strain of 60%. Also, the $m_S Ti_3C_2T_x$- and $m_A Ti_3C_2T_x$-based stretchable flexible SCs retain 78.4 and 74.6% of their initial capacitance after 1000 repeated cycles of stretching strain of 60% under −30 °C, respectively (Figures 7f and S27). Meanwhile, $m_S Ti_3C_2T_x$- and $m_A Ti_3C_2T_x$-based stretchable SCs also exhibit an impressive cycling stability with a capacitance retention of 82.1 and 80.3% over 10000 cycles at −30 °C, respectively (Figure S28). Such an intrinsic and stable stretchability at low temperatures promotes its potential applications in stretchable and wearable electronics toward real-life environments.

3. CONCLUSIONS

To conclude, high-electrochemical-performance, stretchable, arbitrary deformable, and low-temperature tolerant integrated flexible supercapacitors have been developed by the in situ formation of a modified $Ti_3C_2T_x$ hydrogel on the surface of a PAO_{60}-g-$PSBMA_{60}$ ion-conductive hydrogel electrolyte. The as-prepared PAO_{60}-g-$PSBMA_{60}$ ion-conductive hydrogel exhibits a high ionic conductivity of 29.8 S m^{-1} at 25 °C and 3.4 S m^{-1} even at −30 °C, attributed to the abundant hydrophilic and ionic adsorption capacity of amidoxime groups in PAO and zwitterion groups in PSBMA to facilitate the dissociation of the Li salt. The high ionic conductivity mechanism of the hydrogel is proposed based on in situ c-AFM. The $m_S Ti_3C_2T_x$//PAO_{60}-g-$PSBMA_{60}$//$m_S Ti_3C_2T_x$ and $m_A Ti_3C_2T_x$//PAO_{60}-g-$PSBMA_{60}$//$m_A Ti_3C_2T_x$ integrated stretchable flexible SCs are prepared by facile coating of $Ti_3C_2T_x$/PAO_{10}-g-$PSBMA_{10}$ or $Ti_3C_2T_x$/PAO_{60}-$AGE_{1/100}$ dispersion on both surfaces of the PAO_{60}-g-$PSBMA_{60}$ hydrogel

followed by thermal treatment, respectively. Owing to the excellent hydrophilicity and liquidity, a small amount of PAO_{10}-g-$PSBMA_{10}$ and PAO_{60}-$AGE_{1/100}$ dispersion can permeate into the PAO_{60}-g-$PSBMA_{60}$ hydrogel and is tightly linked with the PAO_{60}-g-$PSBMA_{60}$ hydrogel electrolyte and $Ti_3C_2T_x$ electrodes. Thus, as-prepared $m_S Ti_3C_2T_x$- and $m_A Ti_3C_2T_x$-based flexible SCs exhibit excellent antidelamination ability and present a high recoverable tensile stain of 80%, high volumetric capacitances (519 and 517 F cm^{-3}), and excellent electrochemical stability under many types and times of arbitrary deformation. More importantly, the as-prepared SCs present fantastic antifreezing ability. After 1000 times of stretching strain of 60% at −30 °C, the $m_S Ti_3C_2T_x$- and $m_A Ti_3C_2T_x$-based SCs present the capacitance retention of 78.4 and 74.6%, respectively. It is expected that the presented strategy of preparation of a high-ionic-conductivity and antifreezing hydrogel electrolyte through the grafting route can be applied to develop high-performance hydrogel-based materials. The sandwich-like structure integrated hydrogel constructed by the facile drip coating technique can be adopted in energy storage devices and the as-prepared SCs can be practically applied in wearable electrical devices.

4. EXPERIMENTAL SECTION

4.1. Materials. Ti_3AlC_2 MAX powder was purchased from Lianlixin Technology Co., Ltd. (Beijing, China). Polyacrylonitrile (PAN, 99%), allyl glycidyl ether (AGE, 99%), [2-(methacryloyloxy)ethyl]dimethyl-(3-sulfopropyl)ammonium hydroxide (SBMA), hydroxylamine hydrochloride (NH$_2$OH· HCl, 99%), poly(vinyl alcohol) (PVA), and *N,N*-dimethylformamide (DMF, 99.9%) were purchased from Macklin Biochemical Co., Ltd. (Shanghai, China). Sodium hydroxide (NaOH), hydrochloric acid (HCl), sodium carbonate (Na$_2$CO$_3$), tetrabutylammonium hydroxide (TBAOH, 10%), ammonium persulfate (APS), lithium fluoride (LiF), lithium chloride (LiCl), sodium chloride (NaCl), potassium chloride (KCl), magnesium chloride (MgCl$_2$), zinc chloride (ZnCl$_2$), aluminum chloride (AlCl$_3$), and lithium sulfate (Li$_2$SO$_4$) were purchased from Sinopharm Chem. Reagent Co., Ltd. (Beijing, China).

4.2. Synthesis of Poly(amidoxime) (PAO). Poly-(amidoxime) (PAO) was prepared following the procedure in the literature.[48] In brief, NH$_2$OH·HCl (7.80 g) was dissolved in DMF (84.0 mL) in a round-bottom flask heated by a water bath at 45 °C. Na$_2$CO$_3$ (5.42 g) and NaOH (1.36 g) were then added slowly. After stirring for 3 h, PAN (6.00 g) was added for another 30 min, then reacted at 65 °C for 48 h. The reaction mixture was centrifuged, and then the obtained supernatant was dropped into 500 mL of deionized (DI) water to form a white flock precipitate. After washing with the excess DI water, and then filtering and gathering, the product was dried in a vacuum oven at 35 °C for 12 h to obtain the PAO powder.

4.3. Preparation of PAO-*g*-PSBMA Hydrogels. The PAO-*g*-PSBMA hydrogel was prepared as follows: 300 mg of PAO (3.49 mmol) was dissolved in 3 mL of TBAOH (10%) aqueous solution under stirring. 0.041 mL of AGE (0.0349 mmol) was then added and keep stirring for 1 h. Subsequently, the mixture was heated in a water bath at 65 °C for 6 h. After natural cooling, the solution was dialyzed repeatedly for 3 times in DI water (containing 0.1% TBAOH) to reach a pH value of ∼8, and 3 mL of PAO_{60}-$AGE_{1/100}$ solution was obtained. 300 mg of SBMA (1.08 mmol) was dissolved in 1

mL of DI water and added into the above PAO_{60}-$AGE_{1/100}$ solution under stirring for 1 h. 1 mL of APS (6 mg) aqueous solution was then added into the above mixture and then heated at 65 °C for 12 h without stirring to obtain the PAO_{60}-g-$PSBMA_{60}$ hydrogel. For comparison, PAO-g-PSBMA hydrogels with different mass concentrations of PAO, AGE, and SBMA were fabricated and abbreviated as PAO_x-AGE_y-$PSBMA_z$, where x and z are the mass concentrations of PAO and SBMA, respectively, and y is the molar ratio of AGE and PAO. The PAO_{60}/$PSBMA_{60}$ hydrogel was prepared following the same process as PAO_{60}-g-$PSBMA_{60}$ but without adding AGE. The PVA_{120} hydrogel was prepared as per the literature method: 600 mg of PVA was added into 5 mL of DI water and dissolved at 90 °C under magnetic stirring; the PVA solution was sealed and placed in ambient environment for 48 h to obtain the PVA_{120} hydrogel.[6]

4.4. Preparation of $m_A Ti_3 C_2 T_x$/PAO_{60}-g-$PSBMA_{60}$/$m_A Ti_3 C_2 T_x$, $m_S Ti_3 C_2 T_x$/ PAO_{60}-g-$PSBMA_{60}$/$m_S Ti_3 C_2 T_x$ Hydrogels and Construction of Integrated Stretchable Flexible Supercapacitors.

The $Ti_3 C_2 T_x$ MXenes were prepared using the minimally intensive layer delamination (MILD) method.[51] Briefly, 1.0 g of $Ti_3 AlC_2$ powder was added into 20 mL of 9 M HCl solution containing 1.32 g of LiF and stirred under 35 °C for 24 h. Then, the above acidic suspension was washed repeatedly with DI water by centrifugation at 4000 rpm until the supernatant became a colloidal solution. Finally, the product was treated ultrasonically for 30 min and then centrifuged at 3500 rpm for 60 min to get delaminated few-layered $Ti_3 C_2 T_x$ nanosheets. $Ti_3 C_2 T_x$ was redispersed in DI water to reach a concentration of 5 mg mL^{-1}.

The $m_A Ti_3 C_2 T_x$/PAO_{60}-g-$PSBMA_{60}$/$m_A Ti_3 C_2 T_x$ hydrogel was prepared as follows: 6 mL of PAO_{60}-$AGE_{1/100}$ (1 mg) aqueous solution was mixed with 4 mL of as-prepared $Ti_3 C_2 T_x$ (20 mg) dispersion under stirring. The obtained 2 mL $Ti_3 C_2 T_x$/PAO_{60}-$AGE_{1/100}$ ($m_A Ti_3 C_2 T_x$) dispersion was coated on one side of the PAO_{60}-g-$PSBMA_{60}$ hydrogel and heated at 65 °C for 12 h. After natural cooling, the other side of the hydrogel was treated in the same way. The highly integrated $m_A Ti_3 C_2 T_x$/PAO_{60}-g-$PSBMA_{60}$/$m_A Ti_3 C_2 T_x$ sandwich-like structure hydrogel was obtained after cooling. The $m_S Ti_3 C_2 T_x$/PAO_{60}-g-$PSBMA_{60}$/$m_S Ti_3 C_2 T_x$ hydrogel was prepared following the same procedure as $m_A Ti_3 C_2 T_x$/PAO_{60}-g-$PSBMA_{60}$/$m_A Ti_3 C_2 T_x$, but using PAO_{10}-g-$PSBMA_{10}$ (1 mg) as the substitute for PAO_{60}-$AGE_{1/100}$. For comparison, the $m_P Ti_3 C_2 T_x$/PVA_{120}/$m_P Ti_3 C_2 T_x$ hydrogel was prepared by the same procedure as $m_A Ti_3 C_2 T_x$/PAO_{60}-g-$PSBMA_{60}$/$m_A Ti_3 C_2 T_x$, but using the PVA_{120} hydrogel derived from 6 mL PVA (1 mg) solution substitute for the PAO_{60}-g-$PSBMA_{60}$ hydrogel.

The as-prepared $m_A Ti_3 C_2 T_x$/PAO_{60}-g-$PSBMA_{60}$/$m_A Ti_3 C_2 T_x$, $m_S Ti_3 C_2 T_x$/PAO_{60}-g-$PSBMA_{60}$/$m_S Ti_3 C_2 T_x$, and $m_P Ti_3 C_2 T_x$/PVA_{120}/$m_P Ti_3 C_2 T_x$ hydrogels were cut into rectangular-shaped samples (1×2 cm^2) and then soaked in 7 M LiCl for 12 h as $m_A Ti_3 C_2 T_x$//PAO_{60}-g-$PSBMA_{60}$//$m_A Ti_3 C_2 T_x$, $m_S Ti_3 C_2 T_x$//PAO_{60}-g-$PSBMA_{60}$//$m_S Ti_3 C_2 T_x$, and $m_P Ti_3 C_2 T_x$//PVA_{120}//$m_P Ti_3 C_2 T_x$ integrated stretchable flexible supercapacitors.

4.5. Characterization and Measurement.

^{1}H NMR spectra were recorded using a 400 MHz Bruker AVANCE III NMR spectrometer (Karlsruhe, Germany). The X-ray photoelectron spectroscopy (XPS) was performed with a Thermo ESCALAB 250Xi instrument. Fourier transform infrared (FT-IR) spectra were recorded using an IRAffinity-1 spectrometer (Shimadzu, Japan). The atomic force microscope (AFM) measurements were performed in a liquid pool using the Asylum Research MFP-3D microscope by the in situ technique.

4.6. Mechanical Properties Measurements.

The compression and tensile tests were performed using MTS Insight Electromechanical Testing Systems (MTS Systems Corporation). The speed of compression and tensile tests was 0.1 and 0.02 mm min^{-1}, respectively. Cylinder samples with a diameter of 9 mm and height of 5 mm were prepared for the compression tests. Rectangular samples with a length of 25 mm, width of 10 ± 1 mm, and thickness of 30 ± 2 μm were prepared for the tensile tests. For the tensile test, 10 mm of the test sample was clamped to fix.

4.7. Electrochemical Measurements.

The electrochemical performance was characterized using an electrochemical working station (CHI660E, Shanghai, China) and connected with the samples by two Au sheets. Cyclic voltammetry (CV) tests were performed in the scan rate range of 5 to 150 mV s^{-1}. Galvanostatic charge/discharge (GCD) tests were carried out in the current density range of 1 to 20 A g^{-1}. The potential window was 0−1.0 V. Electrochemical impedance spectroscopy (EIS) tests were characterized in the frequency range of 100 kHz to 0.01 Hz and at an amplitude of 10 mV at open circuit potential.

The ionic conductivity was calculated according to eq 1

$$\sigma = \frac{L}{R \times S} \tag{1}$$

where σ is the ionic conductivity, L is the thickness of the hydrogel electrolyte, R is the resistance of the hydrogel electrolyte, and S is the geometric area of the Au sheet and electrolyte interface.

The gravimetric capacitance (C_m, F g^{-1}) of flexible supercapacitors was calculated from the GCD curves by eq 2

$$C_m = \frac{4 \times I \times \Delta t}{m \times \Delta V} \tag{2}$$

The volumetric specific capacitance (C_V, F cm^{-3}) of the electrodes was calculated from the GCD curves by eq 3

$$C_V = C_g \times \rho \tag{3}$$

The volumetric energy density (E_V, Wh L^{-1}) and power density (P_V, W L^{-1}) were calculated according to eqs 4 and 5, respectively

$$E_V = \frac{C^V \times \Delta V^2}{8 \times 3.6} \tag{4}$$

$$P_V = \frac{E^V \times 3600}{\Delta t} \tag{5}$$

where Δt, I, m, ΔV, and ρ are the discharge time (s), discharge current (A), mass of active materials on both electrodes, potential window (V), and density of electrodes (g cm^{-3}), respectively. The density of electrodes was calculated based on eq 6

$$\rho = \frac{m}{Sd} \tag{6}$$

where m, S, and d are the mass (g), area (cm^2), and thickness (cm) of the electrodes, respectively. The densities of

$m_S Ti_3C_2T_x$-, $m_A Ti_3C_2T_x$-, and $m_p Ti_3C_2T_x$-based electrodes are 2.31, 2.32, and 2.14 g cm^{-3}, respectively.

■ ASSOCIATED CONTENT

Ⓢ Supporting Information

The Supporting Information is available free of charge at https://pubs.acs.org/doi/10.1021/acsomega.3c04966.

^1H NMR spectra of PAO and PAO_{60}-$AGE_{1/100}$ powders, AFM amplitude, phase and 3D images of PAO_{60}-g-$PSBMA_{60}$ hydrogel, stress−strain curves and ionic conductivity of PAO_x-AGE_y-$PSBMA_z$ hydrogels, DSC results of PAO_{60}-g-$PSBMA_{60}$ hydrogel, AFM image of $Ti_3C_2T_x$ sheet and $m_S Ti_3C_2T_x$/PAO_{60}-g-$PSBMA_{60}$/$m_S Ti_3C_2T_x$ hydrogel, GCD curves of $m_S Ti_3C_2T_x$ and $m_A Ti_3C_2T_x$ based SCs within 10,000 cycles and arbitrary deformation, cycling tests for 10000 cycles at −30 °C, the table of chemical composition of samples and comparison for ionic conductivity and integrated supercapacitors (PDF)

■ AUTHOR INFORMATION

Corresponding Author

Wenbin Zhong − College of Materials Science and Engineering, Hunan University, Changsha 410082, P. R. China; ◎ orcid.org/0000-0002-1635-2444; Email: wbzhong@hnu.edu.cn

Authors

Zhiyuan Peng − College of Materials Science and Engineering, Hunan University, Changsha 410082, P. R. China; ◎ orcid.org/0000-0001-7164-7811

Yutang Zhou − College of Materials Science and Engineering, Hunan University, Changsha 410082, P. R. China

Honghao Shu − College of Materials Science and Engineering, Hunan University, Changsha 410082, P. R. China

Chuying Yu − College of Materials Science and Engineering, Hunan University, Changsha 410082, P. R. China; ◎ orcid.org/0000-0003-2947-4472

Complete contact information is available at:
https://pubs.acs.org/10.1021/acsomega.3c04966

Notes

The authors declare no competing financial interest.

■ ACKNOWLEDGMENTS

■ REFERENCES

(1) Keum, K.; Kim, J.; Hong, W. S. Y.; Son, J. G.; Lee, S.; Ha, J. S. Flexible/Stretchable Supercapacitors with Novel Functionality for Wearable Electronics. *Adv. Mater.* 2020, 32, No. 2002180.

(2) Lyu, L.; Antink, W. H.; Kim, Y. S.; Kim, C. W.; Hyeon, T.; Piao, Y. Recent Development of Flexible and Stretchable Supercapacitors Using Transition Metal Compounds as Electrode Materials. *Small* 2021, 17, No. 2101974.

(3) Zhu, M.; Ji, S.; Luo, Y.; Zhang, F.; Liu, Z.; Wang, C.; Lv, Z.; Jiang, Y.; Wang, M.; Cui, Z.; Li, G.; Jiang, L.; Liu, Z.; Chen, X. A Mechanically Interlocking Strategy Based on Conductive Micro-bridges for Stretchable Electronics. *Adv. Mater.* 2022, 34, No. 2101339.

(4) Li, Y.; Zhang, J.; Chen, Q.; Xia, X.; Chen, M. Emerging of Heterostructure Materials in Energy Storage: A Review. *Adv. Mater.* 2021, 33, No. 2100855.

(5) Fu, W.; Turcheniuk, K.; Naumov, O.; Mysyk, R.; Wang, F.; Liu, M.; Kim, D.; Ren, X.; Magasinski, A.; Yu, M.; Feng, X.; Wang, Z. L.; Yushin, G. Materials and Technologies for Multifunctional, Flexible or Integrated Supercapacitors and Batteries. *Mater. Today* 2021, 48, 176−197.

(6) Nakhanivej, P.; Yu, X.; Park, S.; Kim, S.; Hong, J.; Kim, H.; Lee, W.; Hwang, J.; Yang, J.; Wolverton, C.; Kong, J.; Chhowalla, M.; Park, H. Revealing Molecular-Level Surface Redox Sites of Controllably Oxidized Black Phosphorus Nanosheets. *Nat. Mater.* 2019, 18, 156−162.

(7) Zhao, Z.; Xia, K.; Hou, Y.; Zhang, Q.; Yead, Z.; Lu, J. Designing Flexible, Smart and Self-sustainable Supercapacitors for Portable/Wearable Electronics: From Conductive Polymers. *Chem. Soc. Rev.* 2021, 50, 12702.

(8) Wang, Y.; Liu, D.; Zhang, Y.; Fan, L.; Ren, Q.; Ma, S.; Zhang, M. Stretchable Temperature-Responsive Multimodal Neuromorphic Electronic Skin with Spontaneous Synaptic Plasticity Recovery. *ACS Nano* 2022, 16, 8283−8293.

(9) Shen, Z.; Zhang, Z.; Zhang, N.; Li, J.; Zhou, P.; Hu, F.; Rong, Y.; Lu, B.; Gu, G. High-Stretchability, Ultralow-Hysteresis Conducting-Polymer Hydrogel Strain Sensors for Soft Machines. *Adv. Mater.* 2022, 34, No. 2203650.

(10) Zhang, Z.; Wang, W.; Jiang, Y.; Wang, Y.; Wu, Y.; Lai, J.; Niu, S.; Xu, C.; Shih, C.; Wang, C.; Yan, H.; Galuska, L.; Prine, N.; Wu, H.; Zhong, D.; Chen, G.; Matsuhisa, N.; Zheng, Y.; Yu, Z.; Wang, Y.; Dauskardt, R.; Gu, X.; Tok, J. B.-H.; Bao, Z. High-Brightness All-polymer Stretchable LED with Charge-trapping Dilution. *Nature* 2022, 603, 624−630.

(11) Jang, B.; Won, S.; Kim, J.; Kim, J.; Oh, M.; Lee, H.; Kim, J. Auxetic Meta-Display: Stretchable Display without Image Distortion. *Adv. Funct. Mater.* 2022, 32, No. 2113299.

(12) Li, L.; Wang, L.; Ye, T.; Peng, H.; Zhang, Y. Stretchable Energy Storage Devices Based on Carbon Materials. *Small* 2021, 17, No. 2005015.

(13) Huang, Y.; Zhong, M.; Shi, F.; Liu, X.; Tang, Z.; Wang, Y.; Huang, Y.; Hou, H.; Xie, X.; Zhi, C. A Polyacrylamide Hydrogel Electrolyte Enabled Intrinsically 1000% Stretchable and 50% Compressible Supercapacitor. *Angew. Chem.* 2017, 129, 9269−9273.

(14) Li, H.; Lv, T.; Sun, H.; Qian, G.; Li, N.; Yao, Y.; Chen, T. Ultrastretchable and Superior Healable Supercapacitors Based on a Double Cross-linked Hydrogel Electrolyte. *Nat. Commun.* 2019, 10, No. 536.

(15) Sun, K.; Feng, E.; Zhao, G.; Peng, H.; Wei, G.; Lv, Y.; Ma, G. A Single Robust Hydrogel Film Based Integrated Flexible Super-capacitor. *ACS Sustainable Chem. Eng.* 2019, 7, 165−173.

(16) Yu, J.; Lu, W.; Pei, S.; Gong, K.; Wang, L.; Meng, L.; Huang, Y.; Smith, J. P.; Booksh, K. S.; Li, Q.; Byun, J.; Oh, Y.; Yan, Y.; Chou, T. Omnidirectionally Stretchable High-Performance Supercapacitor Based on Isotropic Buckled Carbon Nanotube Films. *ACS Nano* 2016, 10, 5204−5211.

(17) Hua, M.; Wu, S.; Jin, Y.; Zhao, Y.; Yao, B.; He, X. Tough-Hydrogel Reinforced Low-Tortuosity Conductive Networks for Stretchable and High-Performance Supercapacitors. *Adv. Mater.* 2021, 33, No. 2100983.

(18) Shao, G.; Yu, R.; Chen, N.; Ye, M.; Liu, X. Y. Stretchable Supercapacitors: From Materials and Structures to Devices. *Small Methods* 2021, 5, No. 2000853.

(19) Chen, C.; Qin, H.; Cong, H.; Yu, S. A Highly Stretchable and Real-Time Healable Supercapacitor. *Adv. Mater.* 2019, 31, No. 1900573.

(20) Jin, X.; Song, L.; Yang, H.; Dai, C.; Xiao, Y.; Zhang, X.; Han, Y.; Bai, C.; Lu, B.; Liu, Q.; Zhao, Y.; Zhang, J.; Zhang, Z.; Qu, L. Stretchable Supercapacitor at −30 °C. *Energy Environ. Sci.* 2021, 14, 3075.

(21) Dai, J.; Qin, H.; Dong, W.; Cong, H.; Yu, S. Autonomous Self-Healing of Highly Stretchable Supercapacitors at All Climates. *Nano Lett.* **2022**, *22*, 6444−6453.

(22) Xu, J.; Jin, R.; Ren, X.; Gao, G. A Wide Temperature-tolerant Hydrogel Electrolyte Mediated by Phosphoric Acid Towards Flexible Supercapacitors. *Chem. Eng. J.* **2021**, *413*, No. 127446.

(23) Liu, Y.; Zhou, H.; Zhou, W.; Meng, S.; Qi, C.; Liu, Z.; Kong, T. Biocompatible, High-Performance, Wet-Adhesive, Stretchable All-Hydrogel Supercapacitor Implant Based on PANI@rGO/MXenes Electrode and Hydrogel Electrolyte. *Adv. Energy Mater.* **2021**, *11*, No. 2101329.

(24) Xiao, F.; Wang, Y.; Wu, Z.; Chen, G.; Yang, F.; Zhu, S.; Siddharth, K.; Kong, Z.; Lu, A.; Li, J.; Zhong, C.; Zhou, Z.; Shao, M. Recent Advances in Electrocatalysts for Proton Exchange Membrane Fuel Cells and Alkaline Membrane Fuel Cells. *Adv. Mater.* **2021**, *33*, No. 2006292.

(25) Gao, G.; Yang, F.; Zhou, F.; He, J.; Lu, W.; Xiao, P.; Yan, H.; Pan, C.; Chen, T.; Wang, Z. L. Bioinspired Self-Healing Human-Machine Interactive Touch Pad with Pressure-Sensitive Adhesiveness on Targeted Substrates. *Adv. Mater.* **2020**, *32*, No. 2004290.

(26) Sutherland, B. R. Charging up Stationary Energy Storage. *Joule* **2019**, *3*, 1−3.

(27) Wang, Z.; Li, H.; Tang, Z.; Liu, Z.; Ruan, Z.; Ma, L.; Yang, Q.; Wang, D.; Zhi, C. Hydrogel Electrolytes for Flexible Aqueous Energy Storage Devices. *Adv. Funct. Mater.* **2018**, *28*, No. 1804560.

(28) Huang, S.; Wan, F.; Bi, S.; Zhu, J.; Niu, Z.; Chen, J. A Self-Healing Integrated All-in-One Zinc-Ion Battery. *Angew. Chem.* **2019**, *131*, 4357−4361.

(29) Li, X.; Yuan, L.; Liu, R.; He, H.; Hao, J.; Lu, Y.; Wang, Y.; Liang, G.; Yuan, G.; Guo, Z. Engineering Textile Electrode and Bacterial Cellulose Nanofiber Reinforced Hydrogel Electrolyte to Enable High-Performance Flexible All-Solid-State Supercapacitors. *Adv. Energy Mater.* **2021**, *11*, No. 2003010.

(30) Shit, A.; Heo, S. B.; In, I.; Park, S. Y. Mineralized Soft and Elastic Polymer Dot Hydrogel for a Flexible Self-Powered Electronic Skin Sensor. *ACS Appl. Mater. Interfaces* **2020**, *12*, 34105−34114.

(31) Zhang, Q.; Hou, X.; Liu, X.; Xie, X.; Duan, L.; Lü, W.; Gao, G. Nucleotide-Tackified Organohydrogel Electrolyte for Environmentally Self-Adaptive Flexible Supercapacitor with Robust Electrolyte/Electrode Interface. *Small* **2021**, *17*, No. 2103091.

(32) Ma, L.; Chen, S.; Wang, D.; Yang, Q.; Mo, F.; Liang, F. G.; Liang, G.; Li, N.; Li, N.; Zhang, H.; Zhang, H.; Zapien, J. A.; Zapien, J. A.; Zhi, C. Super-Stretchable Zinc-Air Batteries Based on an Alkaline-Tolerant Dual-Network Hydrogel Electrolyte. *Adv. Energy Mater.* **2019**, *9*, No. 1803046.

(33) Zhu, X.; Ji, C.; Meng, Q.; Mi, H.; Yang, Q.; Li, Z.; Yang, N.; Qiu, J. Freeze-Tolerant Hydrogel Electrolyte with High Strength for Stable Operation of Flexible Zinc-Ion Hybrid Supercapacitors. *Small* **2022**, *18*, No. 2200055.

(34) Wei, J.; Zhou, J.; Su, S.; Jiang, J.; Feng, J.; Wang, Q. Water-Deactivated Polyelectrolyte Hydrogel Electrolytes for Flexible High-Voltage Supercapacitors. *ChemSusChem* **2018**, *11*, 3410−3415.

(35) Zhao, Y.-H.; Wee, K.; Bai, R. A Novel Electrolyte-Responsive Membrane with Tunable Permeation Selectivity for Protein Purification. *ACS Appl. Mater. Interfaces* **2010**, *2*, 203−211.

(36) Zhang, W.; Guo, F.; Mi, H.; Wu, Z.; Ji, C.; Yang, C.; Qiu, J. Kinetics-Boosted Effect Enabled by Zwitterionic Hydrogel Electrolyte for Highly Reversible Zinc Anode in Zinc-Ion Hybrid Micro-Supercapacitors. *Adv. Energy Mater.* **2022**, *12*, No. 2202219.

(37) Chen, M.; Zhang, Y.; Xing, G.; Chou, S.; Tang, Y. Electrochemical Energy Storage Devices Working in Extreme Conditions. *Energy Environ. Sci.* **2021**, *14*, 3323.

(38) Wu, M.; Wang, X.; Xia, Y.; Zhu, Y.; Zhu, S.; Jia, C.; Guo, W.; Li, Q.; Yan, Q. Z. Stretchable Freezing-Tolerant Triboelectric Nanogenerator and Strain Sensor Based on Transparent, Long-term Stable, and Highly Conductive Gelatin-based Organohydrogel. *Nano Energy* **2022**, *95*, No. 106967.

(39) Mo, F.; Liang, G.; Meng, Q.; Liu, Z.; Li, H.; Fan, J.; Zhi, C. A Flexible Rechargeable Aqueous Zinc Manganese-dioxide Battery Working at −20 °C. *Energy Environ. Sci.* **2013**, *12*, 706−715.

(40) Ying, B.; Chen, R. Z.; Zuo, R.; Li, J.; Liu, X. An Anti-freezing, Ambient-Stable and Highly Stretchable Ionic Skin with Strong Surface Adhesion for Wearable Sensing and Soft Robotics. *Adv. Funct. Mater.* **2021**, *31*, No. 2104665.

(41) Ye, Y.; Zhang, Y.; Chen, Y.; Han, X.; Jiang, F. Cellulose Nanofibrils Enhanced, Strong, Stretchable, Freezing-Tolerant Ionic Conductive Organohydrogel for Multi-Functional Sensors. *Adv. Funct. Mater.* **2020**, *30*, No. 2003430.

(42) Zhang, Y.; Li, T.; Miao, L.; Kaur, P.; Men, S.; Wang, Q.; Gong, X.; Fang, Y.; Zhai, C.; Zhang, S.; Zhang, L.; Ye, L. A Highly Sensitive and Ultra-stretchable Zwitterionic Liquid Hydrogel-based Sensor as Anti-freezing Ionic Skin. *J. Mater. Chem. A* **2022**, *10*, 3970.

(43) Ge, W.; Cao, S.; Yang, Y.; Rojas, O. J.; Wang, X. Nanocellulose/LiCl Systems Enable Conductive and Stretchable Electrolyte Hydrogels with Tolerance to Dehydration and Extreme Cold Conditions. *Chem. Eng. J.* **2021**, *408*, No. 127306.

(44) Wen, J.; Tang, J.; Ning, H.; Hu, N.; Zhu, Y.; Gong, Y.; Xu, C.; Zhao, Q.; Jiang, X.; Hu, X.; Lei, L.; Wu, D.; Huang, T. Multifunctional Ionic Skin with Sensing, UV-Filtering, Water-Retaining, and Anti-Freezing Capabilities. *Adv. Funct. Mater.* **2021**, *31*, No. 2011176.

(45) Wei, J.; Wei, G.; Shang, Y.; Zhou, J.; Wu, C.; Wang, Q. Dissolution−Crystallization Transition within a Polymer Hydrogel for a Processable Ultratough Electrolyte. *Adv. Mater.* **2019**, *31*, No. 1900248.

(46) Yang, J.; Xu, Z.; Wang, J.; Gai, L.; Ji, X.; Jiang, H.; Liu, L. Antifreezing Zwitterionic Hydrogel Electrolyte with High Conductivity of 12.6 mS cm^{-1} at −40 °C through Hydrated Lithium Ion Hopping Migration. *Adv. Funct. Mater.* **2021**, *31*, No. 2009438.

(47) Liu, T.; Xie, Z.; Chen, M.; Tang, S.; Liu, Y.; Wang, J.; Zhang, R.; Wang, H.; Guo, X.; Gu, A.; Yuan, Y.; Wang, N. Mussel-inspired Dual-Crosslinked Polyamidoxime Photothermal Hydrogel with Enhanced Mechanical Strength for Highly Efficient and Selective Uranium Extraction from Seawater. *Chem. Eng. J.* **2022**, *430*, No. 133182.

(48) Yan, B.; Ma, C.; Gao, J.; Yuan, Y.; Wang, N. An Ion-Crosslinked Supramolecular Hydrogel for Ultrahigh and Fast Uranium Recovery from Seawater. *Adv. Mater.* **2020**, *32*, No. 1906615.

(49) Shi, S.; Li, B.; Qian, Y.; Mei, P.; Wang, N. A Simple and Universal Strategy to Construct Robust and Anti-Biofouling Amidoxime Aerogels for Enhanced Uranium Extraction from Seawater. *Chem. Eng. J.* **2020**, *397*, No. 125337.

(50) Guo, X.; Lu, Y.; Fu, D.; Yu, C.; Yang, X.; Zhong, W. Ultrahigh Ionic Conductivity and Alkaline Tolerance of Poly (amidoxime)-based Hydrogel for High Performance Piezoresistive Sensor. *Chem. Eng. J.* **2023**, *452*, No. 139208.

(51) Alhabeb, M.; Maleski, K.; Anasori, B.; Lelyukh, P.; Clark, L.; Sin, S.; Gogotsi, Y. Guidelines for Synthesis and Processing of Two-Dimensional Titanium Carbide (Ti$_3$C$_2$T$_x$ MXene). *Chem. Mater.* **2017**, *29*, 7633−7644.

(52) Ren, J.; Liu, Y.; Wang, Z.; Chen, S.; Ma, Y.; Wei, H.; Lü, S. An Anti-Swellable Hydrogel Strain Sensor for Underwater Motion Detection. *Adv. Funct. Mater.* **2022**, *32*, No. 2107404.

(53) Wu, S.; Hua, M.; Alsaid, Y.; Du, Y.; Ma, Y.; Zhao, Y.; Lo, C.; Wang, C.; Wu, D.; Yao, B.; Strzalka, J.; Zhou, H.; Zhu, X.; He, X. Poly(vinyl alcohol) Hydrogels with Broad-Range Tunable Mechanical Properties via the Hofmeister Effect. *Adv. Mater.* **2021**, *33*, No. 2007829.

(54) Liu, T.-C.; Sutarsis, S.; Zhong, X.; Lin, W.; Chou, S.; Kirana, N.; Huang, P.; Lo, Y.; Chang, J.; Wu, P.; Chen, S. An Interfacial Wetting Water based Hydrogel Electrolyte for High-Voltage Flexible Quasi Solid-State Supercapacitors. *Energy Storage Mater.* **2021**, *38*, 489−498.

(55) Zheng, J.; Tan, G.; Shan, P.; Liu, T.; Hu, J.; Feng, Y.; Yang, L.; Zhang, M.; Chen, Z.; Liu, Y.; Lu, J.; Neuefeind, J. C.; Ren, Y.; Amine, K.; Wang, L.; Xu, K.; Pan, F. Understanding Thermodynamic and

Kinetic Contributions in Expanding the Stability Window of Aqueous Electrolytes. *Chem* **2018**, *4*, 2872−2882.

(56) Liu, R.; Cui, L.; Wang, H.; Chen, Q.; Guan, Y.; Zhang, Y. Tough, Resilient, Adhesive, and Anti-Freezing Hydrogels Cross-Linked with a Macromolecular Cross-Linker for Wearable Strain Sensors. *ACS Appl. Mater. Interfaces* **2021**, *13*, 42052−42062.

(57) Bera, A.; Chandel, A. K. S.; Kumar, C. U.; Jewrajka, S. K. Degradable/Cytocompatible and pH Responsive Amphiphilic Conetwork Gels based on Agarose-Graft Copolymers and Polycaprolactone. *J. Mater. Chem. B* **2015**, *3*, 8548−8557.

(58) Wang, D.; Russell, T. P. Advances in Atomic Force Microscopy for Probing Polymer Structure and Properties. *Macromolecules* **2018**, *51*, 3−24.

(59) Zhao, Y.; Wang, L.; Zhou, Y.; Liang, Z.; Tavajohi, N.; Li, B.; Li, T. Solid Polymer Electrolytes with High Conductivity and Transference Number of Li Ions for Li-Based Rechargeable Batteries. *Adv. Sci.* **2021**, *8*, No. 2003675.

(60) Huang, Y.; Xiao, L.; Zhou, J.; Liu, T.; Yan, Y.; Long, S.; Li, X. Strong Tough Polyampholyte Hydrogels via the Synergistic Effect of Ionic and Metal-Ligand Bonds. *Adv. Funct. Mater.* **2021**, *31*, No. 2103917.

(61) Huang, C.; Tang, Q.; Feng, Q.; Li, Y.; Xu, Y.; Zhang, Y.; Hu, A.; Zhang, S.; Deng, W.; Chen, X. Achieving Ultrahigh Volumetric Performance of Graphene Composite Films by an Outer−Inner Dual Space Utilizing Strategy. *J. Mater. Chem. A* **2020**, *8*, 9661−9669.

(62) Xu, S.; Wei, G.; Li, J.; Han, W.; Gogotsi, Y. Flexible MXene-Graphene Electrodes with High Volumetric Capacitance for Integrated Co-cathode Energy Conversion/Storage Devices. *J. Mater. Chem. A* **2017**, *5*, 17442−17451.

(63) Wang, Y.; Yang, X.; Pandolfo, A. G.; Ding, J.; Li, D. High-Rate and High-Volumetric Capacitance of Compact Graphene-Polyaniline Hydrogel Electrodes. *Adv. Energy Mater.* **2016**, *6*, No. 1600185.

(64) Xu, T.; Yang, D.; Zhang, S.; Zhao, T.; Zhang, M.; Yu, Z.-Z. Antifreezing and Stretchable All-Gel-State Supercapacitor with Enhanced Capacitances Established by Graphene/PEDOT-Polyvinyl Alcohol Hydrogel Fibers with Dual Networks. *Carbon* **2021**, *171*, 201−210.